DEPARTMENT OF PHYSICS
UNIVERSITY OF JYVÄSKYLÄ

CALIBRATION OF THE BONE MINERAL DENSITY SCALE ON X-RAY MICROTOMOGRAPHY

JALMARI PIRHONEN

Thesis for the Degree of
Licentiate of Philosophy

UNIVERSITY OF JYVÄSKYLÄ

Jyväskylä, Finland
April 2016

Abstract

Over the past decade, development of X-ray microtomography has critically improved the research of bone structure. Microtomography permits three-dimensional assessment and determination of structural parameters, such as the bone volume fraction, porosity, pore orientation, pore size distribution, and mapping of the localized bone mineral content. In the contrary, traditional methods for such analysis have relied on combining data e.g. from scanning electron microscopy (for two-dimensional microscopic structure imaging) and ashing and scale measurements (for determining the bone mineral content). Microtomographic assessment can be carried out simultaneously in single bone sample, which was not possible with the traditional techniques. Determination of the bone mineral content with X-ray microtomography requires calibration of the X-ray absorption scale by introducing samples, i.e. phantoms, with known bone mineral densities in the same imaging volume with the bone. The bone mineral content scale is then fixed relying on a linear relationship between absorption and (mineral) density. It is not possible, however, to use commercially available phantoms (a few millimeter dimensions) with high (sub-micrometer) imaging resolutions now available on X-ray microtomographs, since the field of view in this case is small (e.g. 1 mm). The objective of this thesis is to address the problem of size limitation by introducing a new phantom based on a paste-like material. The paste is composed of hydroxyapatite powder and ultraviolet light curing adhesive. It can be applied at small portions to make thin coatings on the bone sample, so as to minimize the volume required for the phantom. The results indicate that the proposed phantom is reproducible and temporally stable. The phantoms exhibit a comparable or better accuracy of bone mineral content assessment as compared to commercially available phantoms. Importantly, it is shown that a three-phase phantom tested on a small bone sample (1 mm diameter) features a good accuracy of bone mineral content assessment. Results of this thesis thereby permit using desktop X-ray microtomographs for bone mineral content mapping at sub-micrometer resolution.

JYFL Laboratory Report 2/2016
ISBN 978-951-39-6549-5 (nid.)
ISBN 978-951-39-6550-1 (PDF)
ISSN 0357-9344

Preface

The work presented in this thesis was conducted at the Department of Physics at the University of Jyväskylä in 2013-2016. The research project was funded by the Finnish Cultural Foundation, Central Finland Regional fund (Suomen Kulttuurirahaston Keski-Suomen rahasto), Jenny and Antti Wihuri Foundation (Jenny ja Antti Wihurin Rahasto) and University of Jyväskylä, for all of which I wish to express my gratitude.

I wish to thank my supervisors, Dr. Petro Moilanen, who has guided me in all of my scientific contributions throughout these years and Prof. Jussi Timonen for ultimate leadership. I give my gratitude also for the whole tomography group, who has given me great aid and support, the Department of Chemistry for lending equipment and materials, fellow graduate students and especially the personnel working at the office of the Physics Department. You all make magic happen.

I address special thanks to the almighty people of the FL 353 Holvi, whom I have witnessed to become an international network of magnificent scientists. Even when the Titans fall, let us stand unite.

Mum and dad, thank you for supporting me with your neverending love and care. And finally for my wife Karoliina: no words can express my gratitude for you watching this thing through with me. Without you none of this would have happened.

Contents

Glossary

µCT Microtomography
3D Three-dimensional
aBMC Areal bone mineral content
aBMD Areal bone mineral density
BMC Bone mineral content
BMD Bone mineral density
cc Cubic centimeters, cm^3
CCD Charge-coupled device
CdTe Cardmium telluride
CV Coefficient of variation
DXA Dual-energy X-ray absorptiometry
FBP Filtered back projection algorithm
FOV Field of view
GV Grey value
HAp Hydroxyapatite
PBS Phosphate buffered saline
POM Polyxymethylene plastic
PTH Parathyroid hormone
QCT Quantitative computed tomography
RMS Root mean square
SD Standard deviation
SE Standard error
SEM Scanning electron microscopy
SR Synchrotron radiation
TV Total volume
UV Ultraviolet
W Tungsten
WHO World Health Organization
YAM Young adult mean

Chapter 1

Introduction

Material research has risen to one of the most important fields in the physics. Although new substances and compounds are seldom found and the interactions in macromolecular world may be well known, moving to the microscopic length scale changes the entire situation. Modern imaging techniques permit assessment of the inner structure of materials and structures by extremely high resolutions (up to 50 nm length scale) and provide answers to unresolved questions revealing new phenomena. X-ray imaging has been used in material sciences for decades but only during the 21^{st} century the hardware and applications have evolved to a state where research can be made without investing billions of dollars to a large facility. Today, compact X-ray based computed tomography devices are available and in active use around the world.

Osteoporotic fractures are vastly increasing in numbers due to the growing lifespan of elderly population and changing lifestyle in terms of poor diet and low physical exercise in general [1]. Worldwide, osteoporosis causes more than 8.9 million fractures annually of which 3.5 million happens in the EU (2010, [2]) where the cost of osteoporosis is estimated to be €37 billion, and with estimated increase of 28 % by 2025. Normally the bone mass increases through childhood and the peak is achieved in young adulthood, after which bone undergoes natural resorption. The degree of resorption process is highly individual and dependent on many aspects such as lifestyle and genetic stress. A high rate of resorption causes structural alterations to one's bone matrix. These alterations affect the geometrical (cortical thickness and cross-section area) and material (stiffness, mineral density and porosity) properties of bone [3]. Osteoporosis is diagnosed when the threshold bone mineral density (BMD) is measured to be critically lower comparing to the healthy young adult population.

The diagnostics of osteoporosis is based on clinical assessment of the global bone mineral content in several skeletal sites, and is obtained by

detecting X-ray absorption with the so-called *dual-energy X-ray absorption* (DXA) method. This method relies on the recorded two dimensional projection of the whole body or specific body part, e.g. arm or leg. Three dimensional (3D) absorption measurements such as *quantitative computed tomography* (QCT) benefit on the well defined volumes instead of the 2D projections. A set of calibration phantoms is placed next to the imaged volume (e.g. inside the structures of the patient couch) and a common clinical CT device or smaller peripheral QCT device can then be used to measure BMD at selected parts. Although the volumetric precision in these devices is much better compared to the DXA method, the radiation dose to the patient as well as the cost of these devices are much higher. Also the resolution (300 μm,[4]) is not enough for small objects. In the contrary, research of the microscopic details of bone structure (e.g. porosity and localized mapping of bone mineral density) requires using destructive methods.

X-ray based microtomography is able to reveal geometric structures in ultrahigh resolution (sub micrometer scale). However, calibration is required in order to obtain information on also the mineral content [5, 6]. Whenever bone mineral density has been studied, most of the studies have been done in larger length scale (about 5 μm) [7]. A more elaborate review of the literature concerning bone microtomography is given in Section 3.3. Earlier observations of mineral densities using ultrahigh resolution have been restricted by the width of the imaging window which is only one millimeter wide and usually is filled fully by the imaging target whereby no additional phantoms could be placed in the same view. Solving this problem is the key issue of this study, which is a continuum to the author's previous work where the advantages of microtomography (μCT) imaging were evaluated and the microstructure of cortical bone samples were studied [8]. Similarly in this study a μCT device found at the tomography laboratory at the Department of Physics, University of Jyväskylä, is used to determine mineral density of a cortical bone sample. Thus far the limitation has been in the field of view (FOV) where it is practically impossible to locate any commercial phantoms, due to the narrowness of the window, to calibrate the grey scale levels to mineral densities.

The objective of this research is to develop a new calibration phantom to permit localized estimation of the mineral density of cortical bone tissue in ultrahigh resolution μCT scanner with limited field of view. The paste-like phantom is designed to be easily reproducible, made of low cost components and needs to fulfill the following requirements [9]: (a) its X-ray attenuation should be comparable with that of the objects of interest and should cover a representative range of mineral densities and (b) material must be homogenous at the spatial resolution of the scanner.

Chapter 2

Bone and osteoporosis: from macroscopic length scale to microscopic details

2.1 Bone anatomy and structure

The human *skeleton* of an adult contains 213 bones when excluding the sesamoid bones [10]. Bones, together with cartilage, form the *skeletal system*. Its main function, at the organ level, are to protect the vital organs and bone marrow, to provide a solid mechanical frame for the muscles, to enable locomotion and to provide a metabolic reserve for nutrients such as calcium and to provide continuous supply of new blood cells [11, 12]. The skeletal system undergoes continuous change to adapt to one's lifecycle: at childbirth newborn babies have over 270 bones some of which fuse together [10] and many bones increase or decrease the bone mass depending on the changing strain of individual bone.

Bones can be divided in five main categories [10]: long bones, short bones, flat bones, irregular bones and sesamoid bones. Long bones are characterized by a shaft, the diaphysis, which is much longer than its width. Long bones can also be distinguished by the epiphysis, the round shaped head at the end of the shaft [11]. They are mostly round shaped and made of compact *cortical bone* with an inside cavity, the medullary canal, for the *bone marrow* surrounded by *trabecular bone*. Bones found in this category are such as clavicles, radii, femur and tibiae. Short bones are bones that are equally long and wide but still coated with a thin layer of compact bone but forming of mostly trabecular bone. They are located in the hands and feet (carpals and tarsals). Flat bones are structurally like short bones but differ

in shape and size. Most of the larger bones in the skeleton are flat bones such as the skull, scapulae, sternum, ribs and ilium (pelvis) [13]. Their function is to provide broad surfaces for muscular attachment and protect organs extensively. Irregular bones are the ones with peculiar shape that cannot be grouped to any of the former category. They have several functions for protecting soft or nervous tissue and providing anchor points for muscles. Irregular bones are such as vertebræ, sacrum and mandible. Sesamoid bones form within tendons in regions that wrap around bony prominences such as knee cap [14]. Mechanically they serve to protect the tendon from damage and, in some cases, increase the efficiency or mechanical advantage of their associated muscle so they act as pulleys providing smooth surface for tendons to slide over increasing the tendon's ability to transmit muscular forces.

The cortical bone forms the majority of the human skeleton (about 85 %). It is dense and rigid material featuring a mass density of $\rho = 1.7 - -2.0$ g/cm^3 and its stiffness, which can be characterized for example by Young's modulus (12–18 GPa for cortical bone), comes from the material and configuration [15, 16]. Compact bone can be found on the surface of almost any bone. The remaining 15 % of the bone volume is composed of the spongy trabecular bone. Featuring a more ductile structure (Young's modulus 0.04-1 GPa), trabecular bone usually acts as an absorbing filling of bone cavity for its better resistance for shear strain and compression. Coated by cortical bone they form a rigid but flexible body which can absorb impacts without breaking. While cortical bone can be thought as uniform bone mass, trabecular bone is composed of an interconnected network of bone plates, struts and rods surrounded by bone marrow [17]. Bone marrow is the semi-liquid-like substance where the *hematopoiesis*, the production of blood cells, occurs [18]. Cortical and trabecular bone are distinguished by the varying porosity or apparent density (mass/total volume, including pores) [19]. The most notable qualitative difference is in calcification percentage: 80–90 % for cortical and only 15–20 % for trabecular bone. Trabecular bone is metabolically more active than cortical bone. It is also remodeled more often than cortical bone. Thus the mechanical differences come from the microstructure of the bone types although materially they are the same.

Bone has a hierarchical structure of which the distinction at the macroscopic length scale into the cortical and trabecular bone is just the beginning. Microstructural properties determine its physical properties at the macroscopic scale. The cortical bone can be considered a rigid material that is constructed of a smaller integrity called the *Haversian system* [19]. This system contains several *osteons* that surround an empty channel, lon-

gitudinal *Haversian canals* or transverse *Volkmann's channels*, reserved for blood vessels [20]. On the surface of such canals starts the small interconnected network of *canaliculi* that connects the small micrometer scale pores, the *lacunae*, to one another. Lacunae are pores that contain cells called *osteocytes*. They are former bone forming cells (*osteoblasts*), which became trapped in the bone matrix and became calcified [11].

Osteons are roundly shaped structures formed by the concentric *lamellar* system [11]. *Lamellae* are layered mineralized collagen fibers including multiple *fibrils*. The random packing of collagen fibers in lamellae allows the highest density of collagen per unit volume of tissue. In addition to concentric configuration, lamellae can be oriented parallel in the surface of bone or in *interstitial system*, with a cement line separating them from osteons. Fig. 2.1 shows the internal micro and macro structural properties. When the fiber orientation is less organized and no particular pattern is present, it is called *woven bone*. This special type of cortical bone can be found on the healing site of a broken bone, where body first reserves all the building elements near the fracture and in time remodels woven bone to lamellar matrix [19].

At the cellular level bone tissue is composed of materials such as minerals, water, cells and macromolecules such as lipids and sugars [21]. Compounds can be classified into two main categories: organic and inorganic [11, 18]. The organic part includes vast amount of different type fibrous protein chains known as collagen. The basic building block of the bone matrix fiber network is type I collagen [22]. Often they are twisted as 3 000 Å long, right-handed triple helixes and contains covalent cross-links with glycine as the most common base. Other amino acids are proline and alanine for example. Collagen has a relative molecular mass of 255 and has low boiling temperature of about 48 °C. They can be distinguished with ultraviolet-visible spectrometry (for example pepsin has the peak at 233 nm). Commonly known proteins such as starch and gelatin are also present and some of the body's energy reserve is stored in the bone matrix in the form of glycogen. Bone contains also some fat (adipose tissue) that are derived from carboxyl acids and glycerol [23]. Adipose tissue is mainly stored in the (yellow) bone marrow. The inorganic part of bone is constructed of different minerals of which hydroxyapatite (HAp) $Ca_{10}(PO_4)_6(OH)_2$ is the main component with roughly 68 % of the total mass of the bone [18]. HAp is rather dense ($\rho = 3.15$ g/cm^3) and is formed of small plate-like crystals of about 50 x 25 x 2 nm [19]. The calcium-phosphate ratio Ca/P of HAp is 1.67 [24] while in healthy bone matrix the Ca/P is approximately 1.37–1.87. Other minerals include carbon in the form of carbonate (CO_3^{2-}), hydrogen phosphate (HPO_4^{2-}), silicon, zinc, magnesium and copper [19, 22]. The

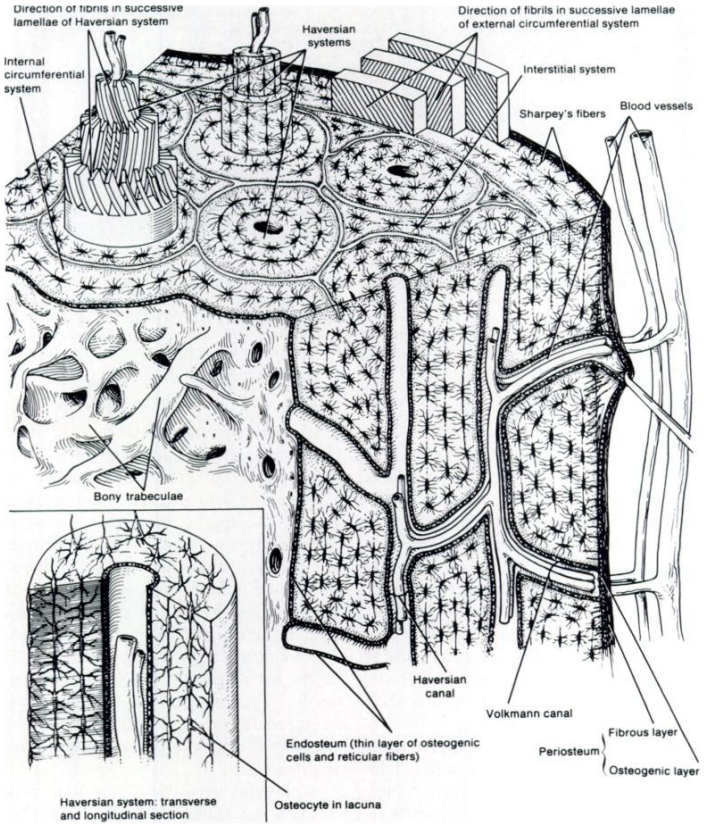

Figure 2.1: The inner structure of cortical bone (after [20]). The Haversian system includes osteons and the intraosseous vascular system. The canaliculi and lacunae spread through bone matrix concentric to osteons. Cement lines separate osteons from one another and from the interstitial systems. Trabecular bone can be seen on the inside of long bone.

combination of organic and inorganic parts gives bone its special features: flexibility, toughness, rigidity and compressive strength.

Bone mass is mainly characterized by the bone mineral density (BMD) which includes the inorganic part of bone compounds. In normal healthy adult bone BMD values are 550–750 milligram per cubic centimeter (cc) and 800–1 300 mg/cc for the trabecular and cortical bone, respectively [25, 26, 27].

The loading capabilities of bone are usually measured quasi-statically i.e. with singular and simplified loading to a uniform direction [28]. This barely has any resemblance to real life situations where bone is being loaded with different forces on multiple directions repetitively. General stiffness of bone

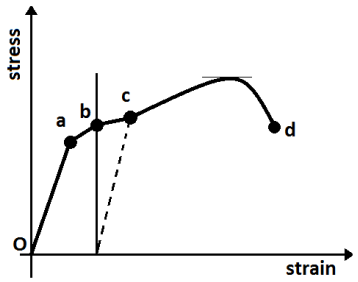

Figure 2.2: A stress-strain curve showing typical yield behavior of a material when stress is applied. The line O–a shows linear behavior that follows Hooke's law and section O–b is reversible and elastic. After point B the reformation becomes irreversible and if the stress is removed the system does not return to its original state (dashed line). When stress is continuously applied (towards point d) at some point system breaks as it collapses to state d.

is measured by Young's modulus and static yield strength. The Young's modulus E, or tensile modulus, can be described with the equation [29], also known as Hooke's law, in terms of stress σ and strain ϵ as

$$E = \frac{\sigma}{\epsilon} = \frac{F/A}{\Delta L/L_0}, \tag{2.1}$$

where F is the force exerted on an object, A is the cross sectional area, L_0 is the original length of the object and ΔL is the change in objects length. In Fig. 2.2 a stress-strain curve is drawn where Hooke's law is applied in the linear section.

2.2 Bone remodeling

Bone remodeling is the process involved in bone growth and turnover and it is a continuous process throughout the lifespan of a person. Remodeling is guided by hormonal activity, nutrient intake and physical activity in terms of adapting to any mechanical needs [30]. For a healthy individual, bones grow in size and mass through the puberty as 90 % of the peak bone mass is acquired by age 18 in girls and 20 in boys. The peak bone mass is then reached at the age of 25–30, where bones have reached their maximum strength and durability. Thereafter a gradual loss of bone mass takes place. For adults bone formation occurs only at sites where resorption has

previously occurred and thus remodeling operates in cycles of activation-resorption-formation sequences [11]. Especially for women, the menopause is a significant milestone in hormonal activity change which affects directly to the bone resorption ratio over forming of bone. Mechanical stimulation, nutritional changes and gene inheritance play also key roles in the bone formation [31].

Bone growth can be described by two main mechanisms, *endochondral ossification* and *intramembranous ossification* [11, 32]. The former is responsible of longitudinal growth, especially for the long bones, featuring continuous formation of new cartilage at a growth region called *physis*. While its diameter stays constant, physis moves along the growth of the bone shaft at the same rate as it mineralizes forming new bone. Intramembranous ossification correlates with the growth in diameter which is needed in flat bones. It is also the main factor in bone modeling and remodeling [11].

Bone remodeling is consequence of the activities of three bone cell types, osteoblasts, osteoclasts and osteocytes. Osteoblasts are responsible of the production of the matrix constituents [11] by forming HAp and other minerals into lamellar structure. They are found lining the bone matrix that they are producing before it is calcified. Osteoclasts on the other hand are cells responsible for bone resorption (Fig. 2.3) and can be located inside the lacunae or on the resorbing bone surface. Osteoclasts resorb bone by acidification and proteolysis of the bone matrix and of the hydroxyapatite crystals encapsulated within the sealing zone of the osteoclast operation area [30]. They digest the HAp crystals from the link to collagen matrix and the residual collagen network is then removed by cathepsins or activated collagenases. What's left is then either reused inside the cell or transported across the cell to be released. The activity of osteoblasts and osteoclasts depends on the signaling osteocytes which control the remodeling cycle.

The amount of calcium in blood circulation and extracellular fluid is monitored by the parathyroid gland [33]. When calcium deficiency is detected the parathyroid gland releases parathyroid hormone (PTH) which stimulates osteoclasts to release calcium from the bone matrix, where 99 % of the bodily calcium is reserved (bones and dentin). This is a direct cause to the activation of bone resorption. The 'cutting cones' of osteoclasts can work up to 500 μm of bone matrix per day. PTH and the calcitriol hormone derived from the vitamin D drives the balance between osteoclastic and osteoblastic activity [30].

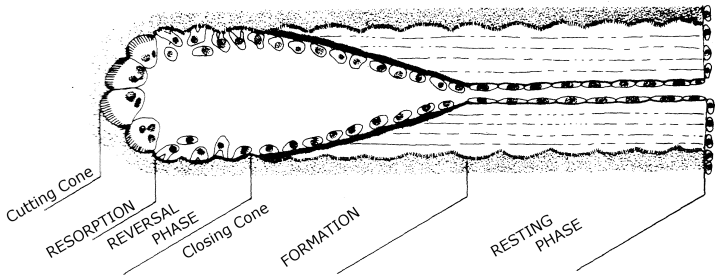

Figure 2.3: Operating osteoclast after [11]. Osteoclasts work as 'cutting cones' as they resorb bone matrix and form new bone at the formation zone where the cone closes.

2.3 Osteoporosis

Osteoporosis is a systematic skeletal disease characterized by low bone density and micro architectural deterioration of bone tissue leading to enhanced bone fragility, and a consequent increase in fracture risk[34]. It is categorized as a metabolic disease for its origin in change of metabolic state including hormonal activity and leading to decrease of bone mass [35]. Micro architectural changes affect the bone properties such as the mineral density, porosity and elasticity. Prior to osteoporosis, osteopenia is a stage where bone properties are recorded to be subject to change but increase in fracture risk can still be regarded as small and preventable.

Osteoporosis results in increasing porosity of the bone mass and decreasing thickness of the cortical wall [36, 37]. Also the outer geometric properties may change [38]. Thus the ability to bear any kind of loading, let it be tensional, compressional or torsional, decreases. Although the single strain rate may stay quite unchanged (Fig. 2.2), continuous strain with traumatical forces yields to osteoporotic fracture as the fatigue damage bearing decreases [38]. At risk are especially bones and bone sites that are under heavy stress such as femoral head or lumbar spine. An example of the difference between healthy and osteoporotic bone has been illustrated in Fig. 2.4.

Osteoporosis can be divided into three separate subcategories depending on the causing factors of bone deterioration: postmenopausal, senile or secondary osteoporosis [39]. The most commonly known is the postmenopausal osteoporosis affecting women between the ages of 50 and 65 years. The largest factor comes from hormonal changes leading to a significant drop in estrogen levels that regulate the bone remodeling cells. Thus osteoblastic activity decreases while osteoclasts remain fully functional re-

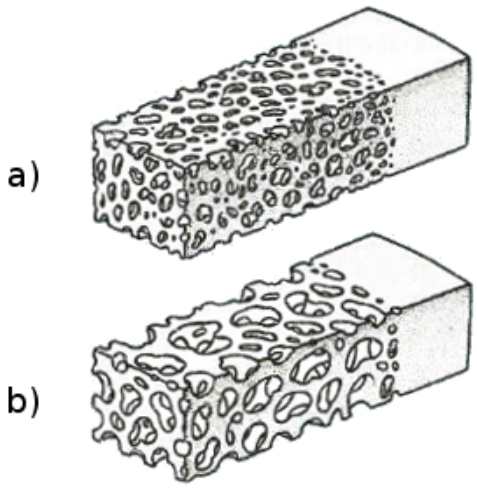

Figure 2.4: (a) Normal healthy bone and (b) osteoporotic bone [12]: A sketch of osteoporotic changes in both cortical and trabecular bone. The cortical wall thickness decreases and the porosity in both cortical and trabecular bone increases.

sulting in remodeling imbalance [38]. Senile osteoporosis affects equally men and women and is considered to be diagnosed mostly after the age of 70 [40]. Secondary osteoporosis is a consequence of chronic conditions that contribute to an accelerated bone loss and thus as no age reference [41]. Commonly known general risk factors for osteoporosis are such as race (white), low calcium or vitamin D intake, low physical activity, low estrogen (female) or testosterone (male) levels and large consumption of alcohol, cigarettes or specific drugs [41, 42, 35].

Osteoporosis is typically characterized by the reduced areal bone mineral density (aBMD) and areal bone mineral content (aBMC), assessed by dual energy X-ray absorptiometry (DXA) [42]. Areal mineral density refers to the amount of mineral per square centimeter of the bone and can be measured from the whole skeleton to give a total estimation of the universal BMD or giving an exact bone specific estimation when measured from a local site where fractures predominantly occur such as hip, lumbar spine or the trochanter of the femur (Fig. 2.5). BMD values (measured by DXA) are used to calculate the T-score which is determined against normative data for young healthy adults and is expressed by [43]

$$T = \frac{X - X_y}{\text{young adult standard deviation}}, \tag{2.2}$$

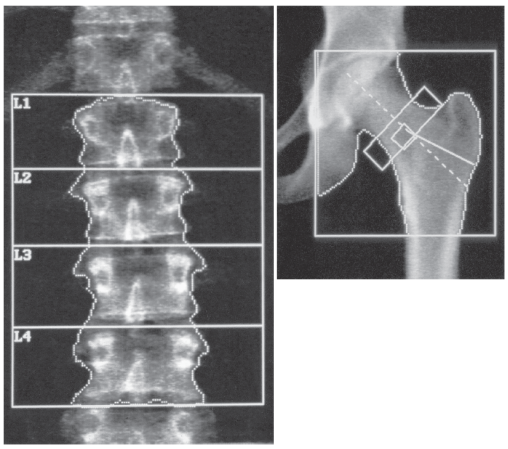

Figure 2.5: Two-dimensional DXA measurement of the lumbar spine and hip in a young healthy adult [42].

where X is the patient's BMD, X_y is the average peak BMD for the healthy young reference population of the same gender and the denominator represents the standard deviation (SD) of the same reference population. T-score enables by definition the comparison between other possible measuring techniques [42]. Criteria made by the World Health Organization (WHO) define the normality and the state of osteoporosis in T-score units as in Table 2.1. The normal age relation can be corrected by using a Z-score [43], which relates the patient's BMD to the normative data for the same age group or race. This is useful especially for the elderly people with normal bone composition for their age.

Throughout the clinical practice DXA is regarded as "golden standard" for which other measuring techniques to assess BMD or BMC are referred. With its acceptable accuracy, stable calibration and relatively low radiation dose induced to the patient it is a decent method, but different techniques are developed and competing against DXA for better assessment of true BMD and better assessment of skeletal status. It must be noted that DXA measures only the 2D projection of the BMD. To name just an example of a rival technique, quantitative ultrasound relies also to the noninvasive method without ionizing radiation exposure to the patient and the results are promising [44].

Table 2.1: WHO criteria for the diagnosis of osteoporosis based on BMD using T-score.

Category	Criteria	T-score
Normal	Values of BMD within 1 standard deviation below the young adult mean (YAM)	≥ -1
Osteopenia, low bone mass	Values of BMD more than 1 SD below the YAM, but less than 2 SD below this value.	< -1 and > -2.5
Osteoporosis	Values of BMD 2.5 SD or more below YAM	≤ -2.5
Severe osteoporosis	Values of BMD 2.5 SD or more below the YAM in the presence of one or more fragility fractures.	

Chapter 3

X-ray imaging

X-rays are considered as electromagnetic radiation within a range of wavelengths from 0.001 nm to 0.1 nm, corresponding to energies of 150 keV to 10 keV, respectively [45]. X-rays are generated when light, or charged high-energy particles lose their speed rapidly when hitting particles of high atomic number, i.e. has a large atomic mass. X-rays penetrate well non-metallic substances and are used in many fields of industry and in clinical studies. X-rays, also commonly known as Röntgen radiation, named after its founder, a German scientist Wilhelm Röntgen in 1895. The story behind this discovery and the first radiograph, a vague shadowgram of the hand of his wife Anna Bertha with the identifiable image of the ring in her finger is one of the most famous stories in science [46].

3.1 Production of X-rays

A common way of producing X-rays is the X-ray tube, which is a glass encased vacuum tube shown in Fig. 3.1 [45]. Current is driven to the cathode where electrons are emitted towards positively charged high density anode usually made of tungsten. This potential difference, known also as the accelerating voltage U, is usually in the range of 15 keV to 150 keV depending on the design. The electron flux can then be expressed by the applying current I and the radiation power as P determined by U and I [45]. Anode material has to have high atomic number to effectively decelerate the impacting electrons as it also has to have high melting point to withstand high temperatures (3 410 °C for tungsten [47]). Anode can be static rod shaped with an inclined surface or it can be a rotating disk to distribute the area of electron impact to a wider area to dissipate heat [45]. The angle of the inclined anode surface is optimized to guide the generated X-rays out of

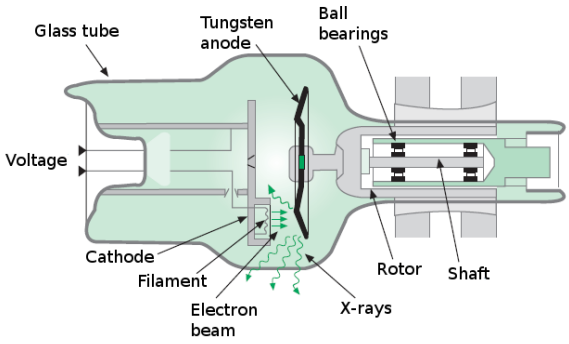

Figure 3.1: A sketch of an X-ray tube with its basic components [45]. Electrons are emitted from the cathode and driven with the accelerating (maximum) voltage towards high density anode, in this case made of tungsten. Only small amount of the energy generated is emitted as X-rays while the rest is emitted as heat. This poses high demands on the heat transfer capabilities of the system.

the tube through a beryllium window towards the target and the detector. Beryllium is a low atomic number (4) alkaline earth metal which has a low absorption coefficient.

X-ray radiation is caused by collisions of the accelerated electrons with the anode. During this event their direction is changed and speed reduced. From the total energy generated, 99 % is transformed into heat and only 1 % converts into electromagnetic radiation due to *bremsstrahlung effect*, which we call X-rays or braking radiation [48]. The spectrum of such radiation is continuous and the maximum energy is dependent on the acceleration voltage inside the X-ray tube (Fig. 3.2). Impacting electrons excite electron states of the anode atoms. Special characteristic radiation observed as notable peaks in the spectrum are the result of anode atoms discharging these excited states on specific atom shells such as K-shell (Fig. 3.4), the innermost electron shell of an atom (Fig. 3.3). In the spectrum this is then called a K-line [45]. Energies of characteristic radiation are unique for each material.

The spectrum radiation power P is given by the equation [45]

$$\frac{\mathrm{d}P}{\mathrm{d}E} = CZI(E_m - E), \tag{3.1}$$

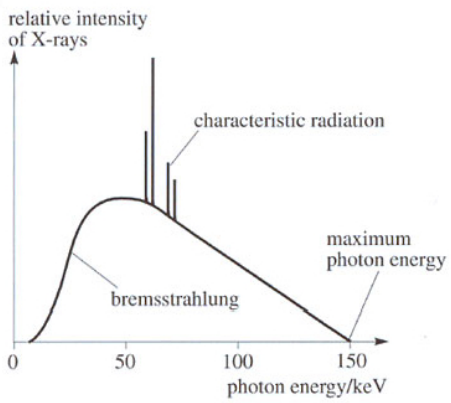

Figure 3.2: A typical energy spectrum of an X-ray tube with a tungsten anode. The characteristic spikes in the spectrum are result of the discharge of electron states in specific shells, such as the K shell visible. The two pairs in this image represent the K_α and K_β spikes.

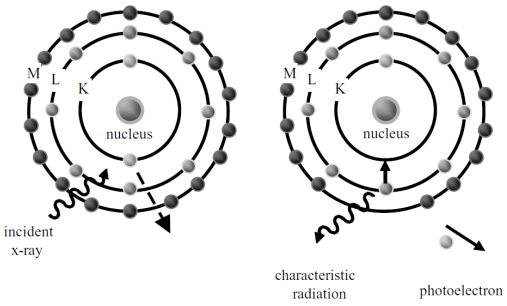

Figure 3.3: Formation of characteristic radiation via photoelectric interaction when an incident X-ray excites a K-shell electron [48].

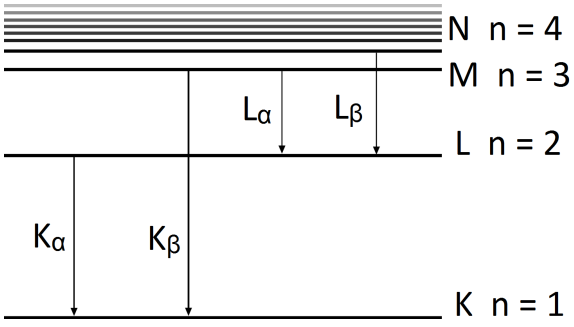

Figure 3.4: A characteristic X-ray is emitted when an electron fills an inner shell. Characteristic X-rays are labeled according to the shell that had the vacancy and the shell from which the electron came [49].

for $0 < E < E_m$, while

$$\frac{\mathrm{d}P}{\mathrm{d}E} = 0 \tag{3.2}$$

if $E > E_m$. In these equations E is the photon energy, E_m is the kinetic energy of the electrons ($E_m = \mathrm{e}\,U$, where e refers to the electron charge), Z is the atomic number of the anode material and C is a constant. Integrating these equations yields

$$P = kZIU^2, \tag{3.3}$$

where $\mathrm{k} = \mathrm{Ce}^2/2$ is a constant.

3.2 X-ray scattering

The interactions between the X-rays passing through material can be divided into three groups [48]: X-rays passing through material and recorded at the detector without any kind of interaction is called primary radiation. Secondary radiation consists of X-rays with altering trajectories scattered by the medium. X-rays can also be absorbed completely by the medium and thus does not reach the detector at all. Similarly to radioactive decomposition of unstable isotopes, the attenuation of the beam is purely a statistical phenomenon which can be expressed by the exponential Beer-Lambert law [50]

$$I = I_0 e^{-\mu(E)d}, \tag{3.4}$$

where I and I_0 are the intensities of the transmitted and incident X-rays, respectively, μ is the linear attenuation coefficient and d is the thickness of the material. The linear attenuation coefficient represents the fraction of a beam of X-rays absorbed per unit thickness of the medium. Scattering phenomena makes the linear attenuation coefficient dependent on the beam energy (Fig. 3.5). The linear attenuation coefficient depends not only on the energy of the material but also on the density, the atomic number and packing of atoms, of the material. Thus a more convenient way of expressing the beams attenuation is the mass attenuation coefficient μ_m (Fig. 3.5). The relation between μ and μ_m is $\mu = \mu_m \rho$ [49].

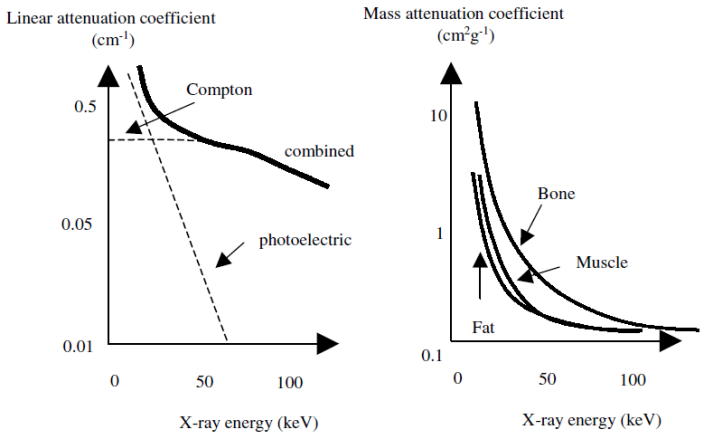

Figure 3.5: Left: Linear attenuation coefficient and the relation between Compton scattering and the photoelectric effect. Linear attenuation coefficient is thus beam energy dependent. Right: Mass attenuation coefficient for various tissue types. For low energies the probability for photoelectric interactions is much higher in bone than in soft tissue due to calcium content of bone. Calcium has a relatively high atomic number compared to soft tissue which has similar mass attenuation coefficient with water [48].

Formation of the secondary radiation is due to three different mechanisms [48]. *Coherent scattering*, or Rayleigh scattering, represents nonionizing interaction between X-rays and an atom. The photon loses its energy to the electron cloud of the atom it is passing through and the energy is converted into oscillation of the electron states. This energy is then released as a subsequent photon with the same wavelength but with random direction. In Fig. 3.5 coherent scattering is not shown due to its small effect. Rayleigh scattering is relevant for only small X-ray energies or in medium with high atomic number.

Compton scattering refers to interaction between an incident X-ray and an electron on the outer shell of an atom. Photon yields some of its energy to the electron which is then ejected from the electron shell. If the X-rays are assumed as unpolarized and the electrons as unaligned the scattering of the X-rays is given by the Klein-Nishina formula [49]

$$\frac{\mathrm{d}\sigma_{KN}}{\mathrm{d}\Omega} = \frac{r_e^2(1+\cos^2\theta)}{2[1+k(1-\cos\theta)]^2}, \tag{3.5}$$

where k $= E/mc^2$, r_e is the classical electron radius and $(d\sigma_{KN})/d\Omega$ is the

differential cross section where $d\Omega$ represents an infinitesimal solid angle element.

The incident beam continues with altered trajectory and different wavelength. This can be described with the equation [51]

$$\Delta\lambda = \frac{2h}{m_e c} \sin^2\left(\frac{\Phi}{2}\right), \tag{3.6}$$

where $\Delta\lambda$ is the change of the wavelength of the beam, h is the Planck constant, m_e is the mass of the ejected electron, c is the speed of light and Φ is the angle of inclination of the beam.

Photoelectric effect is the third of the secondary radiation formation categories. When X-ray is completely absorbed by the medium, a tightly bound electron is emitted from the K or L shell as a photoelectron (Fig. 3.3) [48] with the kinetic energy equal to the differential of the incident photon energy and the binding energy of the electron. The formed empty electron state, or an electron hole, is then filled by a second electron from some higher energy level by releasing the excess energy as characteristic radiation or an *Auger electron*. The energy of the leaving photon is equal to the difference between the binding energy of the outer electron and the emitted photoelectron. The probability of photoelectric attenuation of X-rays decreases significantly as a function of the incident X-ray energy (Fig. 3.5).

3.3 Microtomography

For scientific research, numerous methods are available for the determination of mineral content of calcified tissue. The most direct one is the chemical analysis involving dissolution or ashing of the tissue [52]. This requires total destruction of the sample thus preventing any subsequent measurements and measures only the average mineral content of the destroyed tissue. Other methods include the use of scanning electron microscopy (SEM), confocal laser scanning microscopy and infrared spectroscopy, which are all destructive methods for the sample. Three dimensional microtomography permits visualization and quantification of the inner structures of (non-metallic) materials without destroying the initial sample.

Tomography images are computational reconstructions of multiple absorption images formed by the penetration and attenuation of X-rays inside the sample. Several images, or shadowgrams (Fig. 3.6(a)), are taken of the sample at multiple rotation angles ranging over 180 or 360 degrees. The

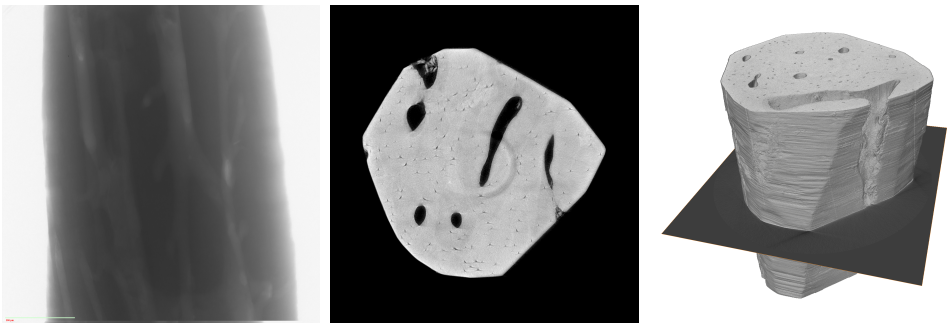

(a) (b) (c)

Figure 3.6: a) An absorption image formed of the X-rays that has penetrated the sample. The dark areas represent more attenuation. A good reconstruction typically requires hundreds of absorption images over an angle interval of at least 180 degrees. The absorption image represents also the field of view of the data acquisition. b) FBP returns the image data as orthogonal slices showing material density as grey values. c) Whole stack of slices rendered as full 3D volume of the scanned sample. The black plane at the bottom of the sample represents the selected slice location of the slice in (b).

quality of the images is dependent on several factors such as the object's dimensions, spatial resolution, magnification, number of imaging angles and exposure time. Shadowgrams are then reconstructed as a stack of cross-sectional 'slices' representing the inner structure of the sample (Fig. 3.6(b)). Reconstruction is usually done according to the filtered back projection algorithm (FBP) which converts the propagation of the X-ray beam into an solvable inversion problem [53, 54]. The correlation between grey value (GV) and the local value of the attenuation follows the Beer-Lambert law and thus a relative scale for the density of the imaged sample can be formed.

All the analysis made on the CT data can now be done when the FBP has been applied to the whole image data and the slice stack has been acquired. Slices can be analyzed as any image with the appropriate image processing software or the image data can be converted as matrices and analyzed numerically. Furthermore the produced slices can be rendered into a 3D model (Fig. 3.6(c)), so as to represent the original 3D geometry.

Microtomographic devices have been extensively used in bone research. Ability to create virtual 3D models of the inner structure of bone without need of decalcification of the sample has been a major advantage as compared to other imaging methods. Morphometric analysis provides structural and architectural information about the imaged object. Both human

and animal bones have been used *ex vivo* and *in vitro* [55, 5, 56]. Moreover, *in vivo* studies have been carried out on animal bones, whereas those on human bones are possible but limited to special equipment and resolutions appropriate for clinical use [57, 58]. When the spatial resolution is at 1 µm level, the lacunae can be identified and the microstructure of cortical bone quantified. Later studies have been able to quantify the micrometer scale network of osteocyte lacunae and the interconnecting canaliculi with both absorption imaging methods as well as with phase contrast [6, 59]. Another topic for multiple studies has been the detailed density analysis in 3D by using microtomography [7, 60]. The objective is to calibrate each voxel to a certain value of density. This field of tomography is not completely trouble-free, since especially the wide X-ray spectrum is a major source of error and three limiting artefacts are present: the beam hardening effect, the partial volume effect and the thickness of the surrounding material [61]. The beam hardening is caused by different attenuation of the low and high energy X-rays and the partial volume effect undermines density values for thin objects because of the attenuation gradient due to scattering effects on the surface of the object. Lastly the surrounding material acts as an additional filter for the penetrating X-rays. Material lying outside the imaged volume, especially if it is unevenly distributed, lowers the density estimation.

Microtomographic devices can be divided into two categories: laboratory scale devices, also called desktop models, and synchrotron radiation (SR) based facilities.

Major differences are the X-ray production method as well as the size and cost of the device. Laboratory scale devices, like the ones used in this work, are relatively cheap and easily available. These devices can be placed in ordinary laboratory space. They typically use X-ray tubes such as the one mentioned in Chapter 3.1 which produces wide energy spectrums, hence the name 'polychromatic µCT'. Sources can be made of different materials (for example silver has been used [62]) to utilize different characteristic radiation. The downside of polychromatic X-rays is the apparent beam hardening effect. Typical to devices of this size is also some degree of instability leading to fluctuating intensity and spectrum. Morphological analysis is not as vulnerable as density analysis for error such as this. Calibration with known density properties can be used to fix the density scale. Often they must, however, be used separately for every imaging. Usually studies focused on the bone mineral density assessment are executed by utilizing SR-µCT [63] that enables the use of an X-ray beam with only a narrow wavelength instead of the whole wide spectrum as in desktop µCT models and with such intensities that the image acquisition can be done in mere

seconds. This removes the problem of the beam hardening effect for example since attenuation has fewer variables. Drawback of SR is that, for now, it can only be produced in large facilities with a suitable particle accelerator and beam line built specifically for X-ray studies. The beamtime is very competitive to obtain.

Chapter 4

Materials and methods

In this study we thus produce a paste-like bone mineral density phantom that permits calibration of the BMD scale in high-resolution X-ray µCT featuring a limited field of view (e.g. ~ 1 mm diameter). For polychromatic X-ray sources phantoms are crucial since the energy spectrum used during imaging is highly dependent on many variables and cannot be precisely controlled even when the parameters are kept constant. For instance the temperature of the source affects on the spot size and thus stability of X-ray production. Commercial phantoms are available ([64, 65] for example) and have been used [66]. These phantoms are either cast on a single piece of epoxy or PMMA (polymethyl methacrylate), or available as a set of separate solid rods. The problem in the case of this study is the size as there is not much external space in the imaging window to fit any solid objects beside the bone sample if the resolution is to be kept at the micrometer scale. The paste-like phantom material can be deposited on the surface of the sample in multiple layers with a total thickness comparable to the diameter of the sample. This helps eliminating the partial volume effect and restricting the beam hardening effect primarily in the phantom volume. The new phantom would allow mineral density assessment using desktop µCT devices that are accessible to smaller laboratories. Such a new phantom could thus avail the bone research significantly.

Common requirements for a phantom material after [9] were: (a) its X-ray attenuation should be comparable with that of the objects of interest and should cover a representative range of mineral densities and (b) material must be homogenous at the spatial resolution of the scanner. Earlier practice has shown that it is not practical to produce phantom with identical BMD values as in cortical bone sample since the production of homogenous phantom paste becomes extremely difficult. In addition, it has been found by experimental procedures that homogeneity of paste-like substances gen-

erally reduces with increasing stiffness. By following requirement (a) HAp is selected to represent the mineral part of the bone and instead of producing similar BMD values as in cortical bone, a linear regression model is fitted on lower values and the estimated cortical bone BMD values are then extrapolated. Requirement (b) will be fulfilled by inspecting the mean density value in terms of grey values (GV) over the phantom volume. With the standard deviation of GV included, this should lead to same density values as with an ideally homogenous paste.

In high resolution imaging the field of view (FOV) is very small and usually the sample takes up the entire imaging area. Thus the phantom should be small enough to be fitted inside the FOV with the sample. The phantom should be inexpensive and relatively easy to reproduce. If the shelf life of the product would appear short the paste needs to be prepared locally and instantly applied on the sample. This requires simplicity of the selected components and the procedure of paste making.

Entire preparation routine is introduced in high detail in the next Section. The reproducibility and stability of the developed recipe is evaluated by several tests (Chapters 5–7). Finally in Chapter 8 three different pastes with known mineral content are fixed on the surface of a cortical bone sample and imaged with a high-resolution microtomograph. A linear regression model is then fitted to the measured grey values representing X-ray attenuation to evaluate the volumetric bone mineral density of the cortical bone sample.

4.1 Development of the phantom paste

Evolution of the preparation process

This section summarizes the phases of testing mixtures of different ingredients for developing the bone mineral density phantom paste.

The idea was first to create a phantom that would be composed of the same elements as the real bone matrix which was why the hydroxyapatite was chosen as the base material. The original idea was to use same proteins as binding element as the bone matrix has. The goal was first set to have the same HAp content than in real bone which is about 68 % [18]. The rest is constructed of water (8 %) and organic matrix (24 %) such as collagen and other proteins.

Protein component was selected by ease of purchase and low cost. After exploring different options, a commercial protein powder was selected: LEADER Palkkari+ consumable protein-carbohydrate drink powder (Lea-

Table 4.1: Protein content of the chosen protein product compared to the compounds found in human skin tissue [67].

Proteins in collagen	In human skin (%)	LEADER Palkkari+ protein powder (%)
Glycine	32.9	2.1
Proline	12.6	6.6
Alanine	10.9	4.3
Hydroxyproline	9.5	—
Glutamic acid	7.4	21.8
Arginine	4.9	3.7
Aspartic acid	4.7	10.2
Serine	3.6	3.9
Lysine	2.9	8.3
Leucine	2.4	9.7
Valine	2.2	5.7
Threonine	1.9	5.4
Phenylalanine	1.3	4.1
Isoleucine	1.1	5.6
Hydroxylysine	0.6	—
Methionine	0.6	2.1
Histidine	0.5	2.3
Tyrosine	0.3	3.5
Cysteine	0.1	1.6
Tryptophan	0	1.2

der Foods OY, Vantaa, Finland). In Table 4.1 are listed the protein content of human skin [67] and the selected protein powder product. It was noted that the content was close enough to try out. In this case glycine was thought to be the most notable difference in the protein content. Amount of glycine could be later increased if the protein was otherwise sufficient as a binding product.

At this point the phantom was intended to be made at site and applied quickly on the sample surface. This led in using ingredients that would set rather quickly after mixing. As an animal based collagen source gelatin was chosen to be the fixing agent of the phantom material. Gelatin is a mixture of peptides and proteins extracted mostly of animal skin or bones

(pig or cow). Many purity grades of gelatin exist for photographic and pharmaceutical use, but here the initial tests were chosen to be completed with common cooking gelatin (Dr. Oetker Gelatinpulver, Dr. Oetker Suomi OY, Helsinki, Finland). Corn starch (Maizena Maissitärkkelys, Unilever, Helsinki, Finland) was selected to substitute starch that is a key component in organic part of the bone matrix. This was thought and later verified to bring viscosity in the paste which would ease the application of the ready paste on the sample.

First phantom trials were designed as 75 % HAp of the dry mass, 22.5 % of collagen including the protein mix and gelatin, and 2.5 % of corn starch of total mass of the dry components. Amount of water was tested progressively from 50 to 80 %. The gelatin was mixed to the heated water until no visible particles were present and the rest of the components were then added to the paste. Ready solution was then applied on a glass capillary and left to solidify and dry.

Evaluating the amount of water in the fixed phantom appeared difficult. This was mainly due to uneven rate of evaporation. The original mass of the dry components actually decreased which meant that part of the water bonded within the powders was also evaporated. An oven was not used to dry the components in fear of breaking the delicate amino acids.

A mortar was also tested to grind the dry components into smaller particles. In Fig. 4.1 is a reconstructed slice of a paste trial imaged with µCT device. As it can be seen from the figure, the mixing of components was challenging to say the least. Gelatin as the binding material was difficult to get evenly distributed. At best the systematical error in homogeneous of the material measured at the grey values in 16-bit depth was about 6 %. As it turned out later for some trials the organic part grew mold and got ruined. These components were left out and new solutions were investigated.

At this point the amount of air bubbles was also an issue since the HAp could be seen to congregate as a denser layer around the bubbles. Several ways of decreasing the air from the paste was considered including changing the mixing style and using a piston or syringe to press the air out. Vacuum was also tested with partial success. Homogeneity of the paste was the next key factor to be focused on.

The binding component was changed from gelatin to agar, a plant based polysaccharide linear polymer used in molecular biology and baking (Amresco Agarose RA Biotechnology grade, code N605-25G, Lot#: 2482C426, Amresco, Solon, Ohio, USA). First the absorption stability was tested with agarose gel between agarose powder content of 0.5–5 % by mass. For four different samples the density of each were inside the standard deviation (for agarose mixtures of 0.5 %, 1 %, 3 % and 5 % by mass at 8-bit depth the

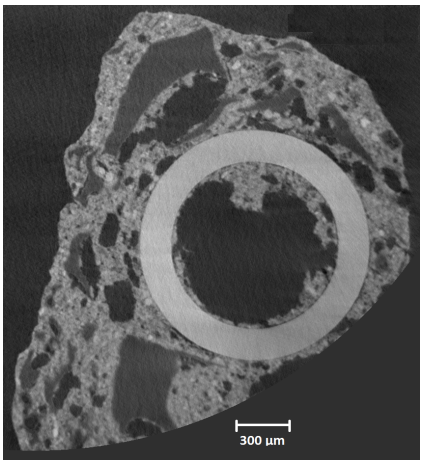

Figure 4.1: A trial paste with 33.3 % of HAp, 50 % of protein mix, 10 % of gelatin and 6.6 % of corn starch mixed with water fixed on a glass capillary. Mixture was not at any satisfying level, large lumps of unmixed gelatin and uneven particles of HAp of size 100 µm can be seen (white spots).

mean grey values were measured as 117±26, 122±27, 126±24 and 115.7±25, respectively) and thus no difference between the agarose content was noted. The result was that the amount of agarose was not significant but the right texture of the phantom paste through changing the agarose content was to be found.

By simplifying the paste content to only the main component HAp and binding component agarose, phantom seemed to work pretty well. It was tested on one bone sample (Fig. 4.2). Paste was functioning as planned, but pastes with different HAp content were difficult to produce, since mineral content was now dependent on the water evaporation.

Next idea was to use binding component that didn't evaporate over time but would be stable after fixing. Several materials were tested in this purpose. A commercial nail polish (Technic nail varnish, Badgequo Ltd. BD20 OEE, England) was first tested as it fastens quite quickly. Liquidity of the polish was adjusted by adding ethyl acetate that is a major component in regular nail polish. The structure of dried nail polish is based on the nitrocellulose after ethyl acetate and N-butyl acetate evaporates. Nitrocellulose can be made in laboratory environment but it has been used as an explosive since 17^{th} century and thus handling of the material is quite hazardous. For safety reasons this material was left outside of this study. Commercial nail polish and ethyl acetate had the same evaporation

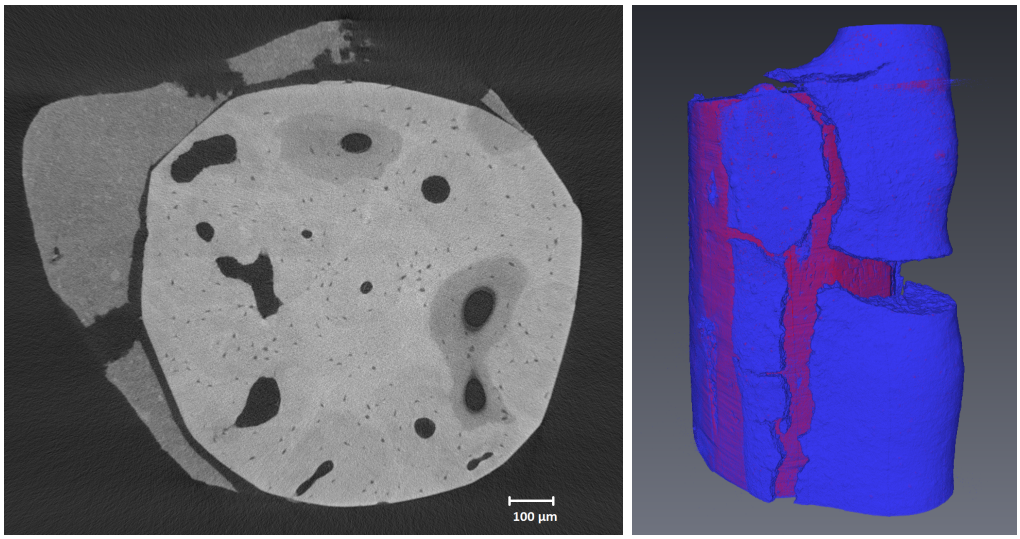

(a) (b)

Figure 4.2: a) Reconstructed slice of BMD calibration phantom trial containing only HAp and agarose. The water has evaporated during long fixing time. Haversian canals and lacunae are clearly visible in the bone. Paste has somewhat homogeneous structure. b) 3D modeled bone sample (colored red) with HAp-agarose calibration phantom paste (colored blue) on the surface. Evaporation of most of the water can be detected as cracked appearance.

dilemma as water-agarose –solution and it was discovered that HAp didn't mix well with ethyl acetate due to the low viscosity of 423 µPa · s [68]. The HAp was noted to sink to the bottom of the mixture vessel or storing vessel in short time.

Development of the mineral density calibration phantom paste was then directed to different glue materials that were easily obtained and known to withstand X-ray radiation and the environment of the scanning chamber. An ultrasonic processor was also introduced in the making of the phantom paste to reduce particle agglomeration and to improve mixing of the HAp into the base material. In Figure 4.3 shown are the X-ray images of the trial phantoms made of beeswax, hot-melt adhesive, ultraviolet (UV) light curing adhesive and nail polish. Ultrasound processing was found to make a difference in the mixing of HAp to the base material as only small unmixed particles are visible while the rest of the powder is somewhat equally distributed over the material, as indicated by the constant shade of grey. The visible particle size was measured from the reconstructed CT-scan data to

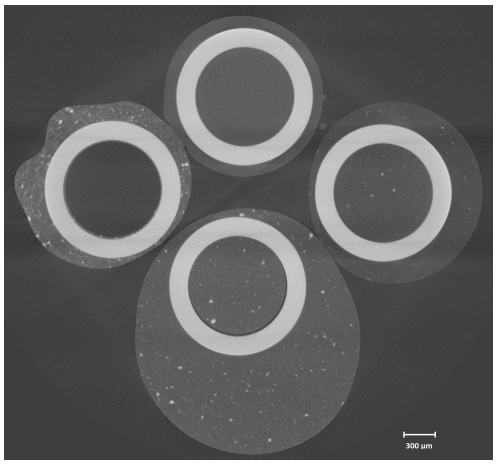

Figure 4.3: An X-ray image of mineral calibration trial phanoms made of hot-melt adhesive (top), ultraviolet light curing adhesive (left), beeswax (right) and nail polish (bottom). Ultrasound processing was utilized for all of the samples.

be roughly 70 µm in diameter.

At this point the UV light curing adhesive was selected for extensive study for its known parameters and ease of processing. As the number of components in the paste was to be minimized, an anti-agglomeration solution was left out of the following trials since the ultrasound processing was found sufficient. A more detailed validation of UV-HAp –phantoms is described in the next section.

Recipe of phantom preparation

Several iterated trials in the previous section finally resulted suitable ingredients and a protocol for phantom preparation. Hydroxyapatite $Ca_5(PO_4)_3(OH)$ was chosen to represent the inorganic component and UV light curing adhesive mimicked the organic part. The mixture of these ingredients provided a uniform and reproducible paste material and permitted the control of BMD based on the known volume fraction of the ingredients mixed. For the UV adhesive, Permabond UV630 (Permabond®, Pottstown, PA, USA, Batch# CJ3184) was used. The Permabond UV630 is a single part, fast setting UV-curable adhesive with the main component being methacrylate ester [69]. As uncured liquid it is clear and colorless while cured with 365–420 nm wavelength UV lamp the color seemed to gain a hint of yellow. This adhesive was chosen for its relatively low viscosity of

200–300 mPa · s and the density was given as 1.1 g/cc, cc denoting as *cubic centimeters* (cm^3).

The hydroxyapatite powder used was a commercial product from Sigma-Aldrich (SIGMA-ALDRICH® Chemie GmbH, Steinheim, Germany). Molecular formula was given as $Ca_5(PO_4)_3OH$ and the molecular weight as 502.31 g/mol. The calculated (calc) and the measured (meas) density of hydroxyapatite is given as $\rho_{\text{calc}} = 3.14$–$3.21$ g/cc and $\rho_{\text{meas}} = 3.16$ g/cc, respectively [70], and for the density in this work a value of 3.163 g/cc was used [71].

An ultrasonic processor Sonics Vibra-cell VCX-750 Watt (Sonics & Materials Inc., Newtown, CT, USA, SN:47348T) was used to mix the ingredients. The ultrasound wave producing tip was changeable from a series of different sizes and shapes. For this work a round tip with the smallest diameter of 5 mm was selected and the minimum amount of liquid of 10 ml was always mixed at a time. The operating instructions of this device advised not to mix too small amounts at a time since the piezoelectric crystal could overheat due to low resistance. This limitation thus regulated the amount of paste prepared per each batch.

For a minimum of 10 ml batch the UV cure was first measured to at least 11 g in a 50 ml decanter glass (VWR1213-1169 borosilicate glass 3.3, VWR, Radnor, PA, USA). Amount of mixed HAp was measured according to the used mass of UV adhesive to produce the required composition. The mass of HAp was determined by

$$m_{HAp} = \frac{v_{UV} \cdot \rho_{HAp} \cdot BMD}{\rho_{HAp} - BMD} = \frac{m_{UV} \cdot \frac{\rho_{HAp}}{\rho_{UV}} \cdot BMD}{\rho_{HAp} - BMD}. \tag{4.1}$$

HAp was then added in the same decanter with the UV adhesive and roughly mixed manually to assure that most of the HAp became wetted by the UV adhesive. This was done to ensure that no powder would separate and possibly 'dust off' during ultrasound mixing. The decanter was then inserted into the mixing chamber and the tip was submerged into the UV adhesive – HAp –mixture. The ultrasound processor was driven at an amplitude of 22 % (representing approximately 72 µm [72]) with a duty cycle of 67 %. This was to ensure that both the crystal and the mixture would not over heat and that the mixture would not cavitate. A cool-down break was also allocated every two minutes to secure that the temperature of the mix would not rise too much and result in an untimely chemical reaction. During this pause the decanter was submerged in cold bath to lower the temperature. It was visually noted that the mixing was efficient to only a small volume around the tip so the location of the tip was changed between

pauses. The total mixing time was in excess of one hour. After mixing the paste was moved to a plastic container made of polyethylene (VWR Amber High-Density Polyethylene Wide Mouth Bottle (30 ml), VWT International, LLC, Radnor, PA, USA) to shield the paste from ambient light.

4.2 X-ray imaging

The detailed imaging in ultrahigh resolution was performed by using the X-radia XCT-400 µCT (Xradia Inc., Concord, CA, USA, Fig. 4.4(a)). The device can be operated with 20–90 keV voltage and 1–8 W power [73]. Minimum spatial resolution that can be achieved with the installed equipment is 1.0 µm with pixel size of 0.3 µm. The detector is a cooled CCD camera with a 2 048 x 2 048 pixel array. The device is located at a temperature and humidity controlled clean environment and the operating computer is fixed to the device with an external arm.

Although the phantom material was developed especially the features of Xradia in mind (e.g. the width of the imaging window when scanning at the sub-micrometer length scale), it does not mean that the phantom is solely for this particular device but can be utilized with any microtomograph.

During development of the phantom material another imaging device was used for its better suitability in imaging multiple samples at once with extensively larger FOV in expense of lower resolution. The Skyscan 1172 (Skyscan Artselaar, Belgium), a small desktop µCT device (Fig. 4.4(b)), was used for initial testing. The device is able to reach a nominal resolution (pixel size) of 1 µm [74]. Operating values for voltage are 20–100 keV with maximum power of 10 W. The special X-ray CCD camera is a 2 300 x 4 000 (10 Mp) cooled CCD sensor with fibre optic coupling to the X-ray scintillator. The device was stationed in a small space shielded from external electromagnetic radiation by metallic walls at the Department of Physics at the University of Jyväskylä. The temperature or the humidity of the imaging room was not specifically controlled but an additional fan was installed to ensure sufficient ventilation. The operating computer was at the regular laboratory environment next to the operating room.

Tuning of the X-ray imaging parameters

Microtomography imaging by X-rays is highly dependent on the energy levels of the X-ray source used. The acceleration voltage determines the maximum energy of the X-ray spectrum. The material then attenuates these energies according to the atoms and especially atomic mass of the

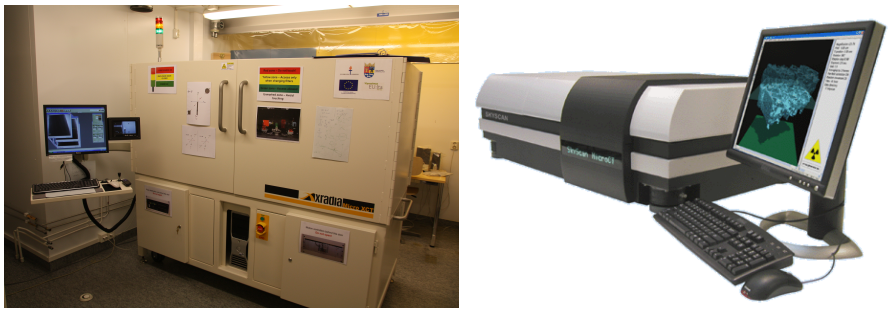

(a) (b)

Figure 4.4: (a) X-radia XCT-400 and (b) Skyscan 1172 [75].

material. For cortical bone this mass attenuation coefficients for different energy levels are shown in Fig. 4.5. The mass attenuation coefficients of HAp according to [76] are shown in Fig. 4.6. The mass attenuations are similar at energies of 1–100 keV which means that majority of the attenuation is caused by HAp that is the main inorganic component in bone. Then again as we can note from the molecular formula of HAp $Ca_5(PO_4)_3(OH)$ the majority of the attenuation is caused by calcium which is the heaviest element present in the HAp platelet. The right-most step shift at 20 keV in Fig. 4.6 is determined by calcium, and the left-most step-shift at 15 keV comes from phosphorus [76].

The characteristic energies of X-ray emission lines for tungsten (W) are listed below [49]. These energies represent the emission lines shown in Fig. 3.2 in Section 3.1.

Element	$K_\alpha 1$	$K_\alpha 2$	$K_\beta 1$	$L_\alpha 1$	$L_\alpha 2$	$L_\beta 1$	$L_\beta 2$	$L_\gamma 1$	$M_\alpha 1$
74 W(eV)	59 318.24	57 981.7	67 244.3	8 397.6	8 335.2	9 672.35	9 961.5	11 285.9	1 775.4

The characteristic emission spectrum of the X-radia XCT-400 µCT device was verified using an Amptek XR-100 spectrometer (Amptek Inc., Bedford, MA, USA). The spectrometer includes a cadmium telluride (CdTe) diode detector with an area of 9 mm^2. The spectrometer was connected to a PX5 digital pulse processor which was then connected to a computer and driven with DppMCA software (version 1,0,0,12; Amptek Inc.). The spectrometer was used with a cooler temperature of 220 K and 700 V high voltage bias. The preamp voltage was set at 8.5 V, peaking time at 2 µs and the signal gain was 12. During measurements a 100 µm aluminium filter was used. The X-ray source of the µCT was set far away (-120 mm) from the axis of rotation (centerline of the sample) to minimize the apparent spot size whereas the sample, when present, was as close to the spectrometer as

possible. Data was collected with the maximum number of channels (8 192) and the device's slow threshold was set to 2.343 % which was detected to be an appropriate level. The energy calibration was done by extracting enough data to identify the $K_\alpha 1$, $K_\alpha 2$, $L_\alpha 1$ and $L_\alpha 2$ spikes to the associated channels 4 716.15, 4 610.69, 783.36 and 676.33, respectively.

The emission spectrum of the tungsten anode of the µCT X-ray source is given in Fig. 4.7. The lowest detected energy was measured at 1.6 keV due to the beryllium windows in both µCT and the spectrometer. The maximum energy measured was 90.03 keV. Beyond this energy level, only noise was detected. As seen from the figure, the characteristic spikes of L and K shells are easily distinguished.

When comparing the emission spectrum of an empty chamber with that imaged through a cortical bone sample we can see that the minerals in bone absorb only the lower part of the spectrum while for higher energy X-rays the emission line stays nearly unchanged (Fig. 4.8). This verifies the absorption coefficient given in Figures 4.5 and 4.6 for cortical bone and hydroxyapatite. Efficient absorption in bone, especially at the energies under 15 keV, can be noted from the absence of the characteristic L spikes in Fig. 4.8.

According to these measurements, any X-rays having the energy above 40 keV encounter only minimal or no attenuation at all. Thus the maximum energy should be limited to gain better contrast when imaging any bone samples or phantoms.

The attenuation behavior of the HAp powder used for the phantom paste was verified by the same principle. A sample made of HAp was produced by mixing 2 grams of HAp powder with 3 grams of 1 % water-agarose solution. The mixture was stirred thoroughly and left to solidify overnight until the excess water had been evaporated and the internal humidity was stabilized at the ambient level. The solid sample was then carved with a scalpel to correspond the dimensions of the cortical bone sample with thickness of about 1 mm. The measured absorption is shown in Fig. 4.9.

As seen from the figure, the absorption of the HAp block is very similar to that of the cortical bone sample featuring a same size. Both of the samples absorbed well energies between 4 and 15 keV. After 26 keV there is practically no absorption in the HAp whereas for cortical bone absorption is evident after 34 keV. The characteristic $L_\alpha 1$–$L_\gamma 1$ spikes at energies of 8.4–11.3 keV are effectively attenuated by the cortical bone while HAp attenuates only part of them while they can still be clearly seen from the spectrum. Cortical bone contains many components i.e. all the organic compounds beside HAp which explains the difference.

This test verifies the correct attenuation behavior of the HAp powder

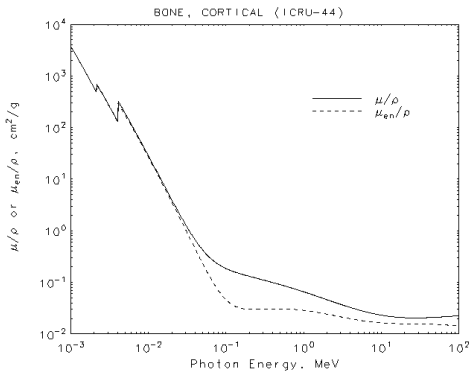

Figure 4.5: The mass attenuation coefficients μ/ρ for cortical bone for energies of 1 keV–100 MeV [77].

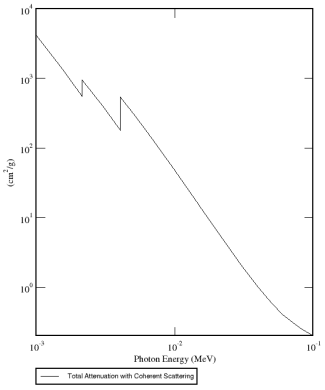

Figure 4.6: The mass attenuation coefficients for HAp for X-ray energies of 1–100 keV [76].

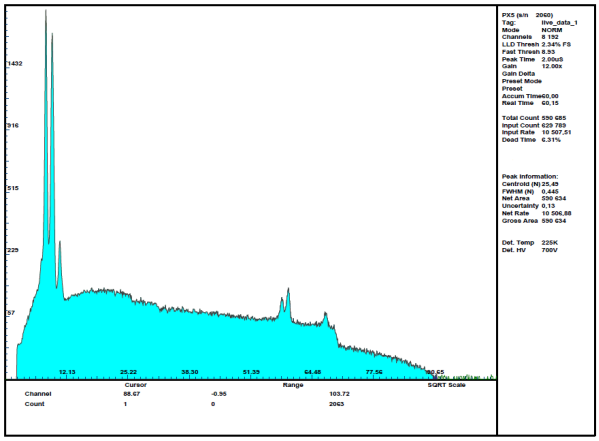

Figure 4.7: Measured emission spectrum of the Xradia MicroXCT-400. Maximum energy of 90 keV was successfully measured and during calibration the characteristic emission spikes of $K_\alpha 1$, $K_\alpha 2$, $L_\alpha 1$ and $L_\alpha 2$ for tungsten were detected. The scale of the Y axis (counts) is shown as proportional to square root for visual purposes.

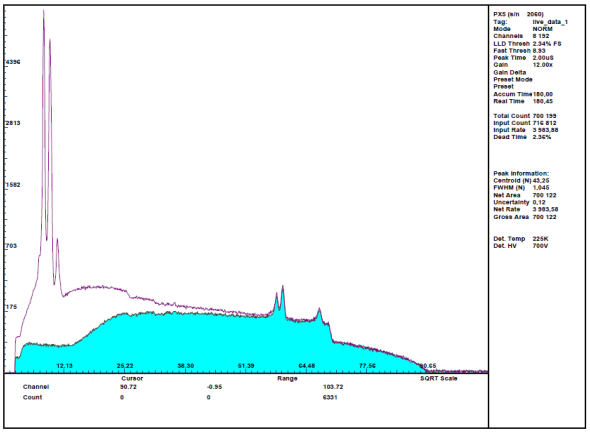

Figure 4.8: The energy spectrum of the X-ray source (purple, same as in Fig. 4.7) and the emission line through a cortical bone sample (green with cyan background). The minerals in bone sample absorb only lower part of the spectrum. The scale of the Y axis (counts) is shown as proportional to square root for visual purposes.

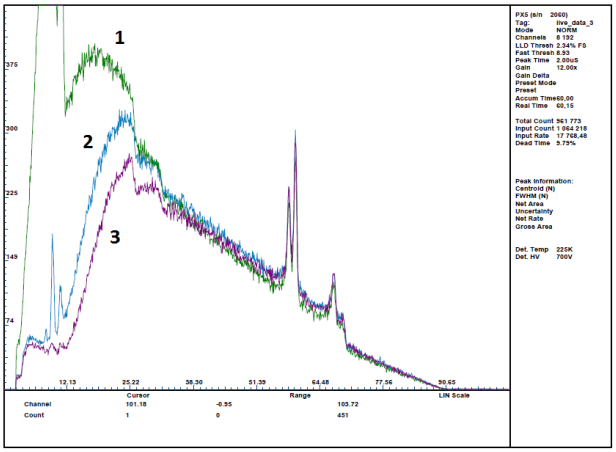

Figure 4.9: X-ray spectrum of the µCT device (1, green), through a sample of HAp-phantom (2, blue) and through a cortical bone sample (3, purple). The characteristic spikes of the icident radiation are left outside of the image for visual reasons (see Fig. 4.7) and the scale is shown as linear. As can be seen, the most absorption for both HAp and cortical bone samples occur at lower energies.

and that most of the cortical bone attenuation properties comes from the HAp which is a major component in the bone matrix. Conclusion of this test is that HAp can be used as a phantom material for its properties similar to cortical bone. The test also ensures the working maximum voltage of the µCT device as there is no need to use voltages over 40 keV since there is no detected absorption above this value. In practice a good contrast in X-ray imaging is achieved when approximately one third of the intensity of X-rays pass the object reaching the detector.

Attenuation properties of a series of glass filters provided by the Xradia manufacturer were also measured with the spectrometer. Specific instructions on how to choose the correct filter for each sample was provided with the filters. Instructions were followed each time Xradia was used. Series contained 12 glass filters to cut off lower energy X-rays and 'harden' the X-ray beam. Filters were numbered from 1 to 6 according to the increasing thickness and labeled as **LE** or **HE** to identify the filters mentioned for lower (20–90 keV) or higher (40–150 keV) energy X-ray source. In this work the lower energy source is used.

Figure 4.10 shows the emission spectrum through some of these filters in comparison with the spectrum where no filter was used. The results indicate that the attenuation increases with increasing thickness of the filter. Only energies below 20 keV are affected for the LE1 when attenuation for LE6 can still be seen for energies over 40 keV. All of the filters affect on the characteristic L-spikes but filters thicker than HE1 seem to affect also to the characteristic K-lines at 58 keV.

The outcome of Fig. 4.10 is that choosing the correct filter is crucial for the results. Without paying much attention it is easy to use too harsh a filter which then attenuates all the energies that would be the most suitable for the scanned sample. Taken for example a sample of soft tissue sensitive to X-rays of 10 to 20 keV would need only the thinnest filter or no filter at all. Practice has shown that when imaging biological samples at the length scale used in this work, filters made of aluminium or copper can be too limiting for the X-ray beam resulting in lower contrast and resolution. For cortical bone and mineral calibration phantoms only the two thinnest filters LE1 and LE2 were used. These were chosen according to the instructions by the manufacturer and the quality of the shadowgrams was endorsed as suitable before the scanning was carried out.

Imaging procedure

For analyzing the quality (reproducibility, temporal stability and homogeneity) of the UV-HAp phantom material, solid phantom rods of size

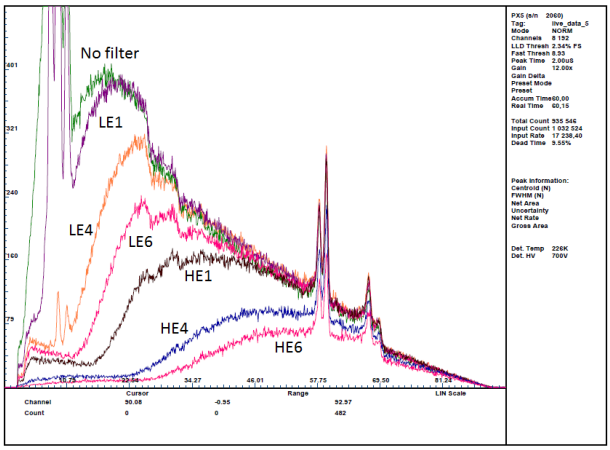

Figure 4.10: X-ray emission lines measured directly from the source without any filter (green) and through selected glass filters (see the color coding). Linear scale is being used.

2 x 2 x 10 mm were prepared by applying small amounts of the mixed paste in molds made of polyxymethylene plastic (POM). POM was chosen since it can withstand many chemicals without unwanted reactions. The paste was fixed with a handheld UV-light for at least 60 s. The prepared rod-shaped phantoms were then imaged together in a plastic container with five commercially available BMD phantom rods with mineral densities of 0, 25, 100, 250 and 750 mg/cc (Computerized Imaging Reference Systems, Inc.,Norfolk, Virginia, USA).

For preliminary testing of the collection of these phantoms, a µCT device Skyscan 1172 (Skyscan Artselaar, Belgium) was used with the following operation values:

Voltage	35 kV
Current	181 µA
Power	6 W
Pixel size	8.4 µm
Exposure time	590 ms
Rotation step	0.10 °
Camera binning	Medium = 2
Camera position	Near
Filter	No
Averaging	10 images
Shift between random movement correction	10 images

More detailed imaging was carried out using the Xradia MicroXCT-400 (Xradia Inc., Concord, CA, USA). The Sample was fixed to the sample holder on the sample stage and the detector lens was driven as close to the sample as possible (with sample specific distances of 4 to 6 mm from the axis of rotation). The X-ray source was driven to 25 mmfrom the rotational axis. Optimal imaging angles for 180° image were calculated by the operating software MicroXCT 7.0.2817 with usual values being from -94° to 94° with a total angle interval of 188°. Imaging was done with high resolution and no pixel combination was used (camera binning 1). Voltage was 30 kV, exposure time per shadowgram was 60 s and reference images were taken 10 times during scanning. Current level and a glass filter were chosen by optimization routine described in a guide distributed by the manufacturer.

Scanning resulted a series of transmission images which were then reconstructed as a 16-bit image stack. Reconstruction was performed with Xradia Reconstructor 7.0.2817 software designed and delivered by the manufacturer. During reconstruction some image enhancing operations were applied. A normal correction for the location of the axis of rotation was performed with pixel center shifting (Fig. 4.11). Roughness due to the hard and dense material was corrected with a standard beam hardening correction (Fig. 4.12). In additon to a hardware based ring artifact correction that was used during scanning, a software based 3-section high contrast ring removal tool was also applied in image reconstruction. Lastly a filter based on the Shepp-Logan function was applied to remove blur.

The finished 16-bit reconstructed image stacks were post-processed in image processing software ImageJ 1.50b (National Institutes of Health, Bethesda, MD, USA). Images were cropped into a more convenient size and background noise was removed by using a 2.0 radius 3D median filter which compensates the GV of each pixel with the adjacent ones. Thus the information lost by using median filter affects only in the range of the spatial resolution (few μm) while objects larger than that, are practically unaffected and the homogeneity can still be measured in the scale of the agglomerates. The effect of the median filter and the enhancement of the fine detail is illustrated in Fig. 4.13. Some samples were then remodeled with Avizo 7.1.0 Fire Edition (Visualization Sciences Group SAS, Burlington, MA, USA) for better visualization.

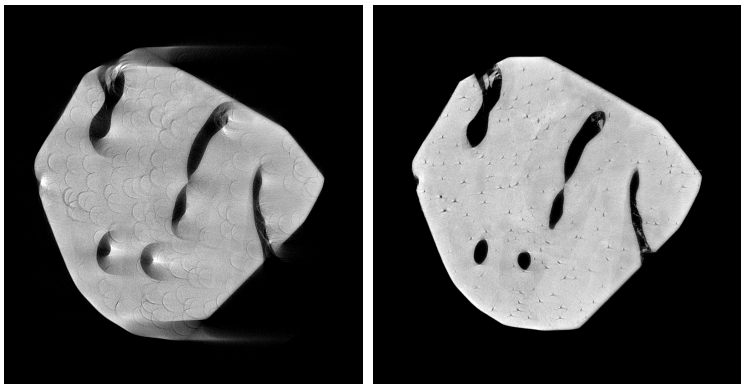

(a) (b)

Figure 4.11: Center shift function was used to correct the location of the axis of rotation. Without correction the geometry of the image slices appear as broken. (a) Misaligned axis of rotation, see especially the top and bottom borderlines of a Haversian canal. (b) Image shows more details when the center shift correction has been applied.

4.3 Bone mineral density estimation from the gray scale levels by linear regression model

The linear regression model is used to evaluate the volumetric bone mineral density using the grey value of the pixels measured with µCT which represents the apparent density of the imaged volume [78]. By adding 3 separate points with known mineral densities we can evaluate the GV of each pixel and get as a result the BMD value of that pixel.

A root-mean-square deviation $s_{y,x}$ of the data from the regression line is characterized by [79]

$$s_{y,x} = \sqrt{\frac{\sum (y - y')^2}{N - 2}}, \tag{4.2}$$

where y is the dependent value, y' is the prediction by linear regression and N is the number of samples.

Confidence limits of the regression line for a given independent value x

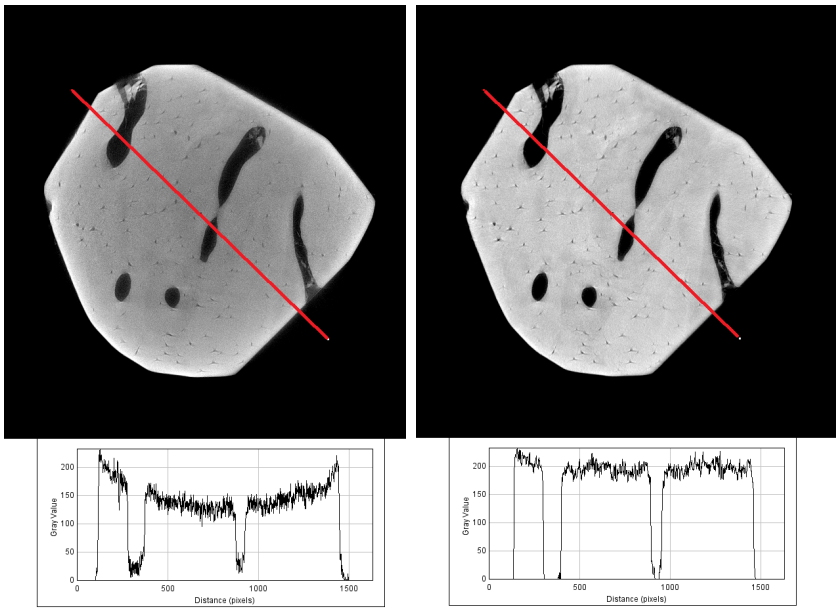

(a) (b)

Figure 4.12: Beam hardening correction was used to correct the uneven attenuation at the edge of the sample (a). Filters were used to remove the low energy photons i.e. 'soft radiation' but a correction was still needed in the reconstruction phase (b). Red line represents the path of the plot profile.

are determined by the standard error of the prediction [79]

$$s_{ye} = \sqrt{\frac{1}{N} + \frac{s_{y,x}^2}{\sum (x_i - \bar{x})^2}}, \tag{4.3}$$

where i is the index of the sum and $\bar{x}$ is the mean value of the x data.

Moreover, confidence limits of a single predicted value for a given value of x are given by

$$s_{ye} = s_{y,x}\sqrt{1 + \frac{1}{N} + \frac{(x - \bar{x})^2}{\sum (x_i - \bar{x})^2}}. \tag{4.4}$$

To characterize the SE of a single predicted term $y_{e(x)}$ when the measurement x is subject to a precision error σ_{ex}, the term $s_{y,x}$ in Eq. 4.4 is

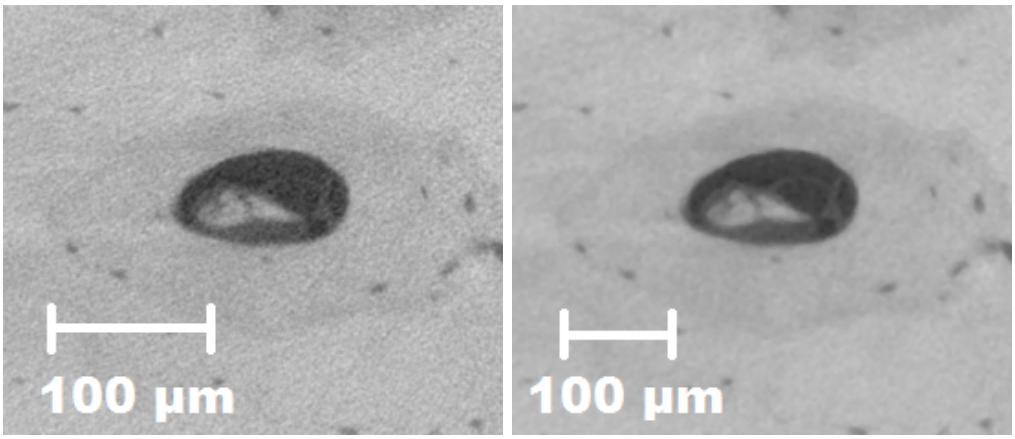

(a) Before denoising (b) Denoised with 2.0 radius median filter

Figure 4.13: The effect of the 2.0 radius median filter for the background noise and detail. Notice the difference in noise levels in air inside a cavity and how small detail, such as the membrane-like substance, can better be recognised. The density information in bone is not affected and the lacunae, diameter approximately 8 µm, are still visible.

replaced by a precision error of the estimate for one measurement, given by

$$s_{y,x'} = \sqrt{s_{y,x}^2 + \frac{\lambda}{1+\lambda}\left(\sigma_{\bar{y}}^2 - s_{y,x}^2\right)}, \tag{4.5}$$

where $\lambda = \sigma_{eq}^2/\sigma_{\bar{x}}^2$ and $\sigma_{\bar{x}}^2$ is the population variance of x.

The SD of the predicted term is expressed by

$$\sigma_y = B\sigma_x = B \cdot SE_x, \tag{4.6}$$

where B is the constant coefficient of the derivative $\frac{dy}{dx}$.

Chapter 5

Substudy I: Reproducibility of phantom preparation

Preparation routine was tested by mixing different batches with the same recipe while maintaining the preparation steps as identical as possible. During this test also the positive effect of using the ultrasonic processor was confirmed by comparing the batches prepared using ultrasonic mixing with one batch of paste prepared with only manual mixing.

Ten batches of phantom paste were mixed according to the procedure described in section 4.1. For each mixed batch a solid rod sample was then fixed by using the POM mold. Additionally one solid sample (s11) was made by using only manual mixing methods to compare the ultrasonically mixed pastes. Total of 11 samples were imaged with a commercial set of 5 BMD calibration phantoms in a plastic vessel with the Skyscan µCT with parameters described in section 4.2. Table 5.1 summarizes the amounts of mixed components and calculated BMD's with the mean grey scale levels determined from the imaged µCT volumes.

5.1 Results

The average GV for samples s1–s10 was 18 126 ± 25 (0.14 %) (Table 5.1). The error bars of GV are thus narrow, which shows that the preparation routine is precise, i.e. the reproducibility is good. For sample s9 a slight miscalculation happened during the preparation which led to decreased BMD value. The sample s11 is excluded for its apparent lower quality due to the manual mixing methods.

The SD column in Table 5.1 represents variability in the grey scale level within each phantom volume imaged. This variability characterizes

Table 5.1: Samples prepared for the preparation stability test. Samples 1–10 are produced by identical preparation routine. Samples a–e are a commercial series of mineral calibration phantoms for reference. UV stands for ultraviolet light curing adhesive, HAp is hydroxyapatite powder, BMD bone mineral density, GV grey value, SD standard deviation, CV coefficient of variation and SE is for standard error. * s11 is mixed with manual methods for comparison.

Sample	Measured UV (g)	Measured HAp (g)	BMD	Mean GV	SD	CV (%)	SE
s1	11.00	1.033	100.01	18 137	904	5.0	0.119
s2	11.02	1.034	100.01	18 166	946	5.2	0.122
s3	11.00	1.033	100.00	18 138	939	5.2	0.122
s4	11.00	1.033	100.00	18 132	943	5.2	0.130
s5	11.01	1.034	100.01	18 140	948	5.2	0.125
s6	11.02	1.034	99.99	18 099	949	5.2	0.121
s7	11.01	1.034	100.00	18 145	1 003	5.5	0.128
s8	11.00	1.033	100.02	18 092	900	5.0	0.108
s9	11.02	1.034	99.97	18 094	946	5.2	0.124
s10	11.01	1.034	100.02	18 115	941	5.2	0.126
s11*	2.16	0.203	99.99	18 094	1 752	9.7	0.234
a			0	15 217	556	3.7	0.162
b			25	15 880	776	4.9	0.178
c			100	18 142	1 344	7.4	0.258
d			250	22 303	1 868	8.4	0.336
e			750	36 149	1 196	3.3	0.214

inhomogeneity of the phantom samples. Inaccuracy related to average GV is characterized by SE, i.e. SD divided by the square root of the number of voxels in the phantom volume. A RMS SE is 0.123 ± 0.006, which means that the average GV per imaged sample has only small inaccuracy due to the large amount of voxels in each of the volumes measured.

Figure 5.1 shows the quality of the imaged samples in detail. A commercial set of calibration phantoms have been included in the image for reference purposes (a–e) (Computerized Imaging Reference Systems, Inc.). A notable remark from is that the prepared HAp paste is even more homogeneous than the commercial reference phantom with similar bone mineral density (sample c, 100 mg/cc). The manually mixed sample s11 is clearly

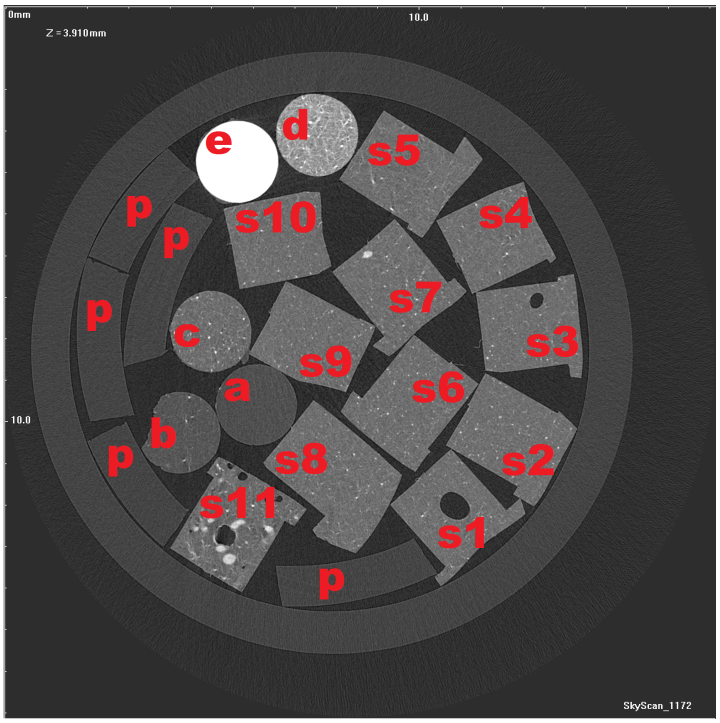

Figure 5.1: Samples s1–s11 with reference samples a–e imaged with Skyscan device. Pieces denoted as "p" are pure plastic only for fixing purposes during scanning.

of lower quality when compared to any other phantom in the image. This is yet another observation supporting the use of ultrasonic processor as antiagglomeration method during mixing.

Fig. 5.2(a) shows the average grey scale level plotted separately for each sample (black color), including results for the reference phantoms (red color). Clearly the quality of the produced phantom paste is better than in the reference phantom when the mean value throughout the solid phantom volume is measured. The manually mixed s11 stands out with larger standard deviation. Fig. 5.2(b) shows linear correlation between the mean gray scale level data and related computational reference BMD for the samples imaged. The gray scale level data was strongly correlated ($R^2 = 0.9987$; $p < 0.001$) with BMD.

This test shows that with the presented methods the phantom paste can be reproducibly prepared, withing an excellent accuracy. There is only a small systematical error present due to the scale used for measuring the contents for each paste batch. Largest error in the mean grey scale level is due to still existing agglomeration that could not be totally removed. This

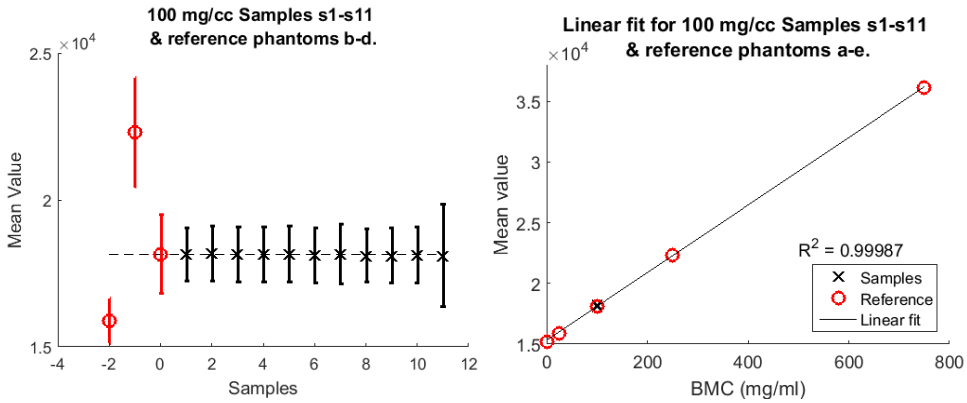

(a) (b)

Figure 5.2: a) The mean grey scale value for phantom paste samples s1-s11 (black symbols) and the reference samples b, c and d (red symbols) (see Table 5.1). The error bars are two standard deviations wide. b) Correlation between mean grey scale value and BMC for all of the samples listed in Table 5.1. Also shown is the linear fit.

test shows that the resolution between different BMD levels is sufficient in the scale of hundreds of milligrams per cubic centimeter.

Chapter 6

Substudy II: Temporal stability of the phantom paste

Stability of the phantom paste over storage time was tested with two different tests. In the first test the effect of a long storage period (from 38 minutes to 10 days) was evaluated for the paste batches prepared in Chapter 5. In the second test, possible changing in the paste material was monitored at several time points within one mixture batch during a 48 hours period.

Paste batches s1 to s10 used in the previous chapter were used to produce solid phantom rods after several days of storage time. During this period the phantom pastes were stored in polyethylene containers that were stored in a stable closet with no movement or any distraction. The samples were then collected with a wooden stick from the top layers of the stored paste to study how the HAp would sink to the bottom of the vessel. The storage time was calculated from the time of creation until fixing the material with the UV lamp. Solid rods were thought as stable ever since. From batch s10 the rods were made on the day of paste preparation, for other batches the storage time was 8 days minimum. These new rods were again placed inside a plastic vessel and imaged with the Skyscan µCT.

For the same scan a block made of pure HAp was tested (Fig. 6.1). The block was made with a hydraulic compressor by measuring 0.3 g of HAp inside a brass cylinder and two steel rods were used to press the HAp as a small tablet with about 2 tons of pressure. The tablet was then carved to the dimensions suitable and equal to the phantom rods.

To evaluate the sinking of the HAp to the bottom of the container vessel with better precision a single patch of ready mixed UV-HAp –phantom paste was chosen to be prepared and followed over time. The paste was designed to contain 100 mg/cc HAp. Each sample was taken from the top layer of the paste.

Table 6.1: Samples prepared for the storage time stability test. Samples s1–s10 are made in identical way after shown storage time. Samples a–e are a commercial set of mineral calibration phantoms for the reference (Computerized Imaging Reference Systems, Inc.). BMD is for bone mineral density, GV for grey value, SD standard deviation and CV for coefficient of variation.

Sample	Storage duration	BMD	Mean GV	SD	CV (%)
s1	10 d	100.01	18 385	1 054	5.7
s2	10 d	100.01	18 258	1 071	5.9
s3	9 d	100.00	18 175	979	5.4
s4	9 d	100.00	18 086	1 154	6.4
s5	9 d	100.01	17 950	1 239	6.9
s6	8 d	99.99	17 979	1 048	5.8
s7	8 d	100.00	18 271	1 123	6.1
s8	8 d	100.02	18 276	936	5.1
s10a	0	100.02	18 481	1 084	5.9
s10b	38 min	100.02	18 366	986	5.4
s10c	135 min	100.02	18 323	940	5.1
s10d	190 min	100.02	18 302	904	4.9
s10e	250 min	100.02	18 274	902	4.9
s10f	283 min	100.02	18 330	931	5.1
a		0	14 948	951	6.4
b		25	16 048	1 061	6.6
c		100	18 267	1 388	7.6
d		250	22 437	1 931	8.6
e		750	36 084	1 331	3.4
HAp		1625	52 817	2 287	4.3

6.1 Results

Test I. For sample batches s1 to s10, the exact storage times for each rod are listed in Table 6.1 with average GV, SD and SE. The imaged samples are shown in Fig. 6.1.

Average GV across the samples is 18 247 ± 151 (0.8 %). Based on Fig. 6.2, the homogeneity of the samples was not as good as in Fig. 5.2 in Chapter 5. Although SD of the average GV is six times higher than average SD of the short term reproducibility, the SD of each sample in this test is only a little higher. Temporal stability of the phantom paste, characterized by

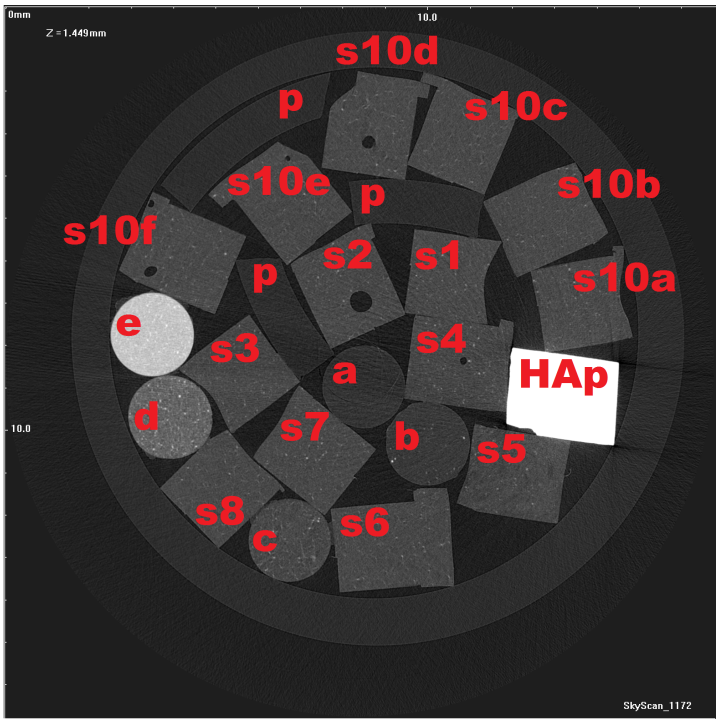

Figure 6.1: Samples s1–s10f imaged with Skyscan device after storage time listed in Table. 6.1 with reference samples a–e. Pieces denoted as "p" are pure plastic only for fixing purposes during scanning. A block noted as "HAp" is a piece of pure HAp.

these error bars, is good. This difference, however, did not affect significantly the SD and SE, characteristic of homogeneity, represented in Tables 5.1 and 6.1.

The mineral density of the pure HAp block was determined to be equal with the mass density which was then determined via weight and volume of the object. The weight was measured to be 0.0724 grams and the volume from the CT scan to be 44.546 mm^3, so the density was then calculated to be $\rho_{HAp} = 1\,625$ mg/cc. This result was then fitted with the rest of the mineral calibration phantoms. As can be seen from Fig. 6.3, the HAp block fits well on the linear regression line with R^2 being 0.9930. This correlation is significant ($p < 0.001$).

Test II. Table 6.2 lists the storage durations and the measurement results for each sample taken from a single mixture batch.

The average grey scale level was $24\,100 \pm 250$. There grey scale level was consistent with storage time, no drifting of the level was observed. Reduction of the level could have been expected due to sinking of the HAp

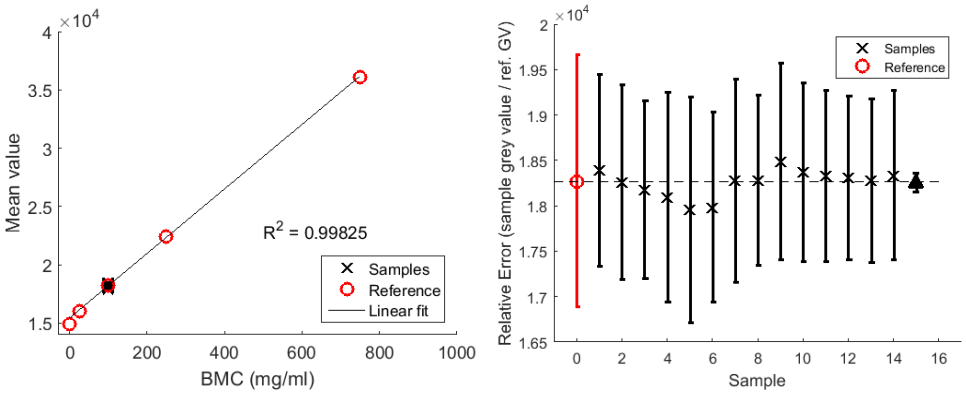

(a) (b)

Figure 6.2: a) Correlation between mean grey scale value and BMC for samples s1–s10 and reference samples a–e. Also shown is the linear fit. b) The mean grey scale value for phantom paste samples s1–s10 (black crosses) with RMS value (black triangle) and reference phantom c (red circle).

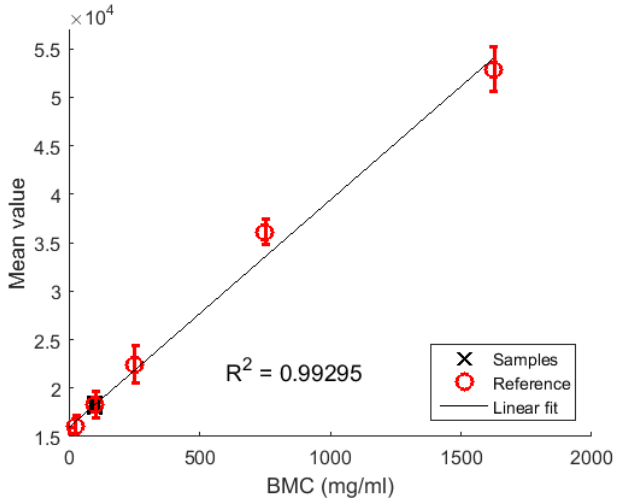

Figure 6.3: Correlation between mean grey scale value and BMC for samples s1–s10, reference samples a–e and a compressed block of pure HAp (top right corner). Linear fit is also shown.

Table 6.2: Data for phantom stability with storage time. Samples have been collected from the top of the batch without mixing the paste. GV is the grey value, SD standard deviation, SE standard error and CV coefficient of variation.

Sample number (#)	Storage duration (hh:mm)	Mean GV	SD	SE	CV (%)
1	0	24 360	1 327	10	5.4
2	0:30	23 903	1 308	16	5.5
3	3:00	23 853	1 368	15	5.7
4	3:50	24 140	1 338	17	5.5
5	5:00	23 954	1 313	9	5.5
6	6:40	24 180	1 313	11	5.4
7	22:30	23 890	1 339	12	5.6
8	27:55	24 025	1 298	14	5.4
9	47:00	24 605	1 368	18	5.6

particles towards the container bottom since the paste was not mixed between preparation of each sample. Random fluctuations in the average grey scale level, characterized by the 250 (1.0 %) error bars, represent good temporal stability with storage time of the paste. This uncertainty is expected to be reduced by careful mixing of the paste each time before extracting a portion for phantom preparation.

The standard deviations in Table 6.2 characterize inhomogeneity of the phantoms, whereas the standard errors represent the error bars of the grey scale average, dependent on the volume size. An RMS standard error of 90 (0.3 %) is small, indicating that the average grey scale level was accurately determined by the prepared phantoms.

These two tests show that during reasonable storing time of 10 days or less no particular difference in sample quality can be detected. Storing was not seen to change the GV value more than other sources of error. Ten days of storage time is relatively short compared to usual experimental time of any scientific work (months). With the acquired results this was seen enough since mixing a new batch of phantom paste took approximately three hours of active work.

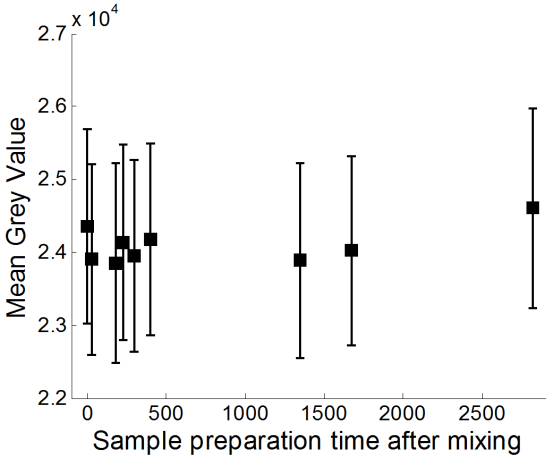

Figure 6.4: Mean grey scale value for samples 1–9 (see Table 6.2).

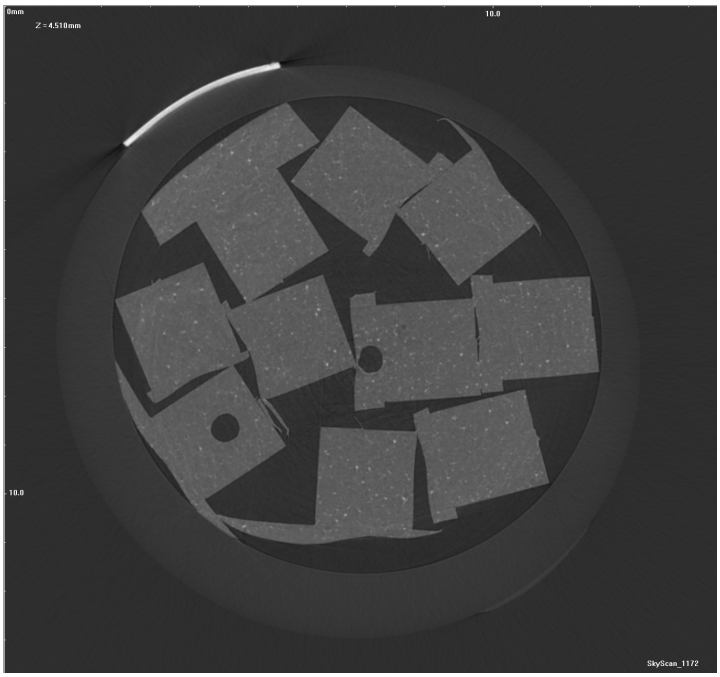

Figure 6.5: A slice of the stack where stability test samples have been imaged with Skyscan µCT. No notable difference can be seen between the samples. The rounding light grey circle is a plastic vessel in which the samples were packed. The bright narrow line is a piece of plastic tape for identification purposes.

Chapter 7

Substudy III: Impact of the phantom volume

Until this point the phantoms prepared and analyzed have been relatively large, consistent in size with the commercial BMD phantoms. However, the objective of this thesis is to create miniature phantoms. In this chapter the impact of the phantom volume on the reliability of related gray scale level assessment is analyzed, so as to determine the volume limit of the new phantoms.

Since the paste is thought to be homogenic and earlier observations have not shown notable inequality except for randomly divided unmixed HAp particles, the method for assessing virtual sub volumes for the phantom paste was selected for its ease and practicality. Beam hardening effect is known to impact on the outer edge of any imaged target and thus reduce usable volume of the phantom material for accurate density calibration. By having a larger volume and splitting it computationally into smaller fractions we could maximize usable phantom volume for this test. This method also allows us to examine extremely small sub volumes which would be highly impractical to apply or cast. The results show the theoretical limit for the systematical error generated by the volume of the phantom material and the impact on the final mineral density measurements can be compared to other sources of errors.

The volume impact was tested in one of the solid phantom rods (s8, Table 5.1) made in Chapter 5. A computational sub-volume analysis was performed for the volume extracted (Fig. 7.1) for the chosen phantom by using MATLAB® (The MathWorks, Inc., Natick, MA, USA). Air was removed by thresholding the extracted volume and subtracting the zero pixels from the volume matrix.

Sub volumes were formed by randomly picking different volume fractions

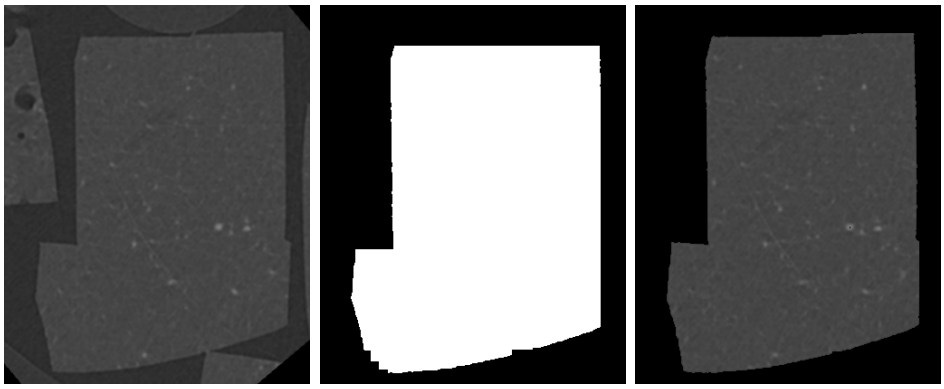

(a) (b) (c)

Figure 7.1: A fixed sample of mineral calibration phantom paste (a) was digitally isolated (b) from other samples and by thresholding the air was removed from the image (c). The pixel values for black space are zero and these were not included in the sub volume.

of the total volume (TV). The mean grey scale level was calculated for each sub volume and this procedure was iterated one hundred times for each volume fraction. Mean grey scale level and the standard deviation were then calculated for the sub volumes.

7.1 Results

Fig. 7.2 and Table 7.1 shows the results of sub-volume analysis. The average gray scale level of a hundred iterations is nearly unaffected by the volume size, whereas the standard error of the gray scale level increases with decreasing sub volume. The standard error of GV becomes noticeable at volumes smaller than $1 \cdot 10^{-5}$ cc. The size of such a volume is comparable to a cubic dimension of 0.22 mm. The standard error of GV is approximately 1 % even for the smallest sub volume of $4.7 \cdot 10^{-8}$ cc (47 μm^3). The actual phantom volume featured by applying paste coating on the surface of a bone surface in Section 8.2 is of the order of 0.1 mm^3 ($1 \cdot 10^{-4}$ cc). Based on this sub-volume analysis, the phantoms gray scale level is appropriately represented in practical situations when the field of view of high-resolution microtomography is 1 mm or even smaller.

Distribution of the grey scale levels in sub volumes of any size inspected here stays constant and follows the normal (Gaussian) distribution. Histograms of the explored volumes were studied for several random generated

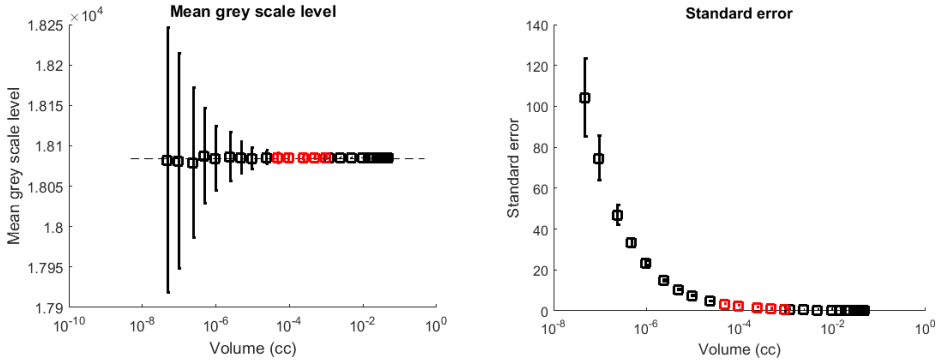

(a) (b)

Figure 7.2: a) Mean grey value with respect to sub volume size. Error bars represent RMS standard deviation of the mean grey scale level within 100 iterations. b) Related standard error with respect to sub-volume size. Orders of magnitude for practical volumes for a 1 mm field of view are highlighted with color red.

samples. A histogram of two differently sized examples can be seen in Fig. 7.3. Since the distribution stays unchanged although the size of the sub volume is decreased, the RMS of the standard deviation stays also unchanged. This is followed by the significant increase in the confidence interval when the sub volume is decreased enough. The inaccuracy of the determination of the GV becomes dominating when the standard error increases to the same order of magnitude as the standard deviation. In this test this happens only to the two smallest sub volumes and thus may be seen as negligible since the volumes used in the following chapter are clearly much larger.

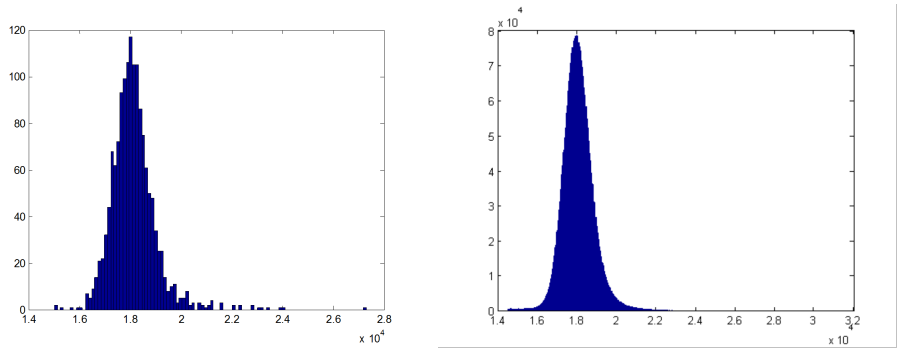

(a) (b)

Figure 7.3: a) A histogram of a sub volume of $9.43 \cdot 10^{-7}$ cc which is a lot smaller than the practical volumes used in the following chapter. The histogram follows normal distribution even when the sub volume contains only few thousand pixels of the total volume. b) For comparison a histogram including 1/10 of the total volume on the left side including almost 10 million pixels. Note that the peak (mean) value is about the same in both cases.

Table 7.1: Data for the sub volumes measured from one of the solid rod samples. The total volume is shown on the first line of the table (100 %). The interesting volumes considering later results are marked with an asterisk (*). RMS stands for root-mean-square, SD standard deviation and SE standard error.

Volume fraction (%)	Volume (pixels)	Volume (cc)	RMS of means	SD	SE
100	$7.44 \cdot 10^7$	$4.72 \cdot 10^{-2}$	18 085	902	0.10 ± 0
90	$6.69 \cdot 10^7$	$4.25 \cdot 10^{-2}$	18 085	902	$0.11 \pm 9 \cdot 10^{-6}$
80	$5.95 \cdot 10^7$	$3.77 \cdot 10^{-2}$	18 085	902	$0.12 \pm 1.3 \cdot 10^{-5}$
70	$5.21 \cdot 10^7$	$3.30 \cdot 10^{-2}$	18 085	902	$0.13 \pm 2 \cdot 10^{-5}$
60	$4.46 \cdot 10^7$	$2.83 \cdot 10^{-2}$	18 085	902	$0.14 \pm 3 \cdot 10^{-5}$
50	$3.72 \cdot 10^7$	$2.36 \cdot 10^{-2}$	18 085	902	$0.15 \pm 4 \cdot 10^{-5}$
40	$2.97 \cdot 10^7$	$1.89 \cdot 10^{-2}$	18 085	902	$0.17 \pm 5 \cdot 10^{-5}$
30	$2.23 \cdot 10^7$	$1.42 \cdot 10^{-2}$	18 085	902	$0.19 \pm 6 \cdot 10^{-5}$
20	$1.49 \cdot 10^7$	$9.44 \cdot 10^{-3}$	18 085	902	$0.23 \pm 1.1 \cdot 10^{-4}$
10	$7.44 \cdot 10^6$	$4.72 \cdot 10^{-3}$	18 085	902	$0.33 \pm 3 \cdot 10^{-4}$
5.0	$3.72 \cdot 10^6$	$2.36 \cdot 10^{-3}$	18 085	902	$0.47 \pm 5 \cdot 10^{-4}$
2.5	$1.86 \cdot 10^6$	$1.18 \cdot 10^{-3}$	18 085	902	$0.66 \pm 1 \cdot 10^{-3}$
* 2.0	$1.49 \cdot 10^6$	$9.44 \cdot 10^{-4}$	18 085	902	$0.74 \pm 1.2 \cdot 10^{-3}$
* 1.0	$7.44 \cdot 10^5$	$4.72 \cdot 10^{-4}$	18 085	902	$1.05 \pm 2 \cdot 10^{-3}$
* 0.5	$3.72 \cdot 10^5$	$2.36 \cdot 10^{-4}$	18 085	903	$1.48 \pm 5 \cdot 10^{-3}$
* 0.2	$1.49 \cdot 10^5$	$9.44 \cdot 10^{-5}$	18 085	902	2.34 ± 0.01
* 0.1	$7.44 \cdot 10^4$	$4.72 \cdot 10^{-5}$	18 085	903	3.31 ± 0.02
0.05	$3.72 \cdot 10^4$	$2.36 \cdot 10^{-5}$	18 085	902	4.68 ± 0.04
0.02	$1.49 \cdot 10^4$	$9.44 \cdot 10^{-6}$	18 084	901	7.19 ± 0.11
0.01	$7.44 \cdot 10^3$	$4.72 \cdot 10^{-6}$	18 085	902	10.5 ± 0.3
0.005	$3.72 \cdot 10^3$	$2.36 \cdot 10^{-6}$	18 086	902	14.8 ± 0.5
0.002	$1.49 \cdot 10^3$	$9.43 \cdot 10^{-7}$	18 084	899	23.3 ± 1.1
0.001	743	$4.71 \cdot 10^{-7}$	18 087	903	33.1 ± 3
0.0005	371	$2.35 \cdot 10^{-7}$	18 079	897	47 ± 5
0.0002	148	$9.39 \cdot 10^{-8}$	18 081	906	75 ± 11
0.0001	74	$4.69 \cdot 10^{-8}$	18 082	897	104 ± 20

Chapter 8

Estimation of bone mineral density

Linear correlation between the grey scale level and BMD permits calibration of the BMD scale by linear regression model. The model is first used on test phantoms to verify the functionality of the method. After this validation, the BMD estimation method is tested on a real cortical bone sample coated by the phantom paste developed.

8.1 Validation

To validate the method of BMD estimation, a series of different phantom paste batches containing five different BMD levels were mixed according to the methods described in Section 4.1. The batches were mixed to an even distribution of powder to liquid ratio (P/L) of 0, 25, 100, 250 and 500 mg/ml leading to BMD values of 0, 24.8, 96.9, 231.7 and 431.7 mg/cc respectively. Three different solid rods were cast from each of the paste batch, except for 0 value which is pure UV resin and thought to be uniform, to estimate the reproducibility in spite of the fact that this had already been explored in Chapter 5. These phantom rods were then imaged together with the same commercial phantom series used earilier. The imaging was performed by Skyscan µCT and the imaging parameters were chosen suitable for the whole set consistently with details given in Chapter 5. The samples' specifications are listed in Table 8.1 and a slice of the reconstruction of the imaged set is shown in Fig. 8.1.

For convenience the bone mineral densities for several samples are merged into one result as a mean value of the GV. The final parameter values (data) used for linear regression model are expressed in Table 8.2.

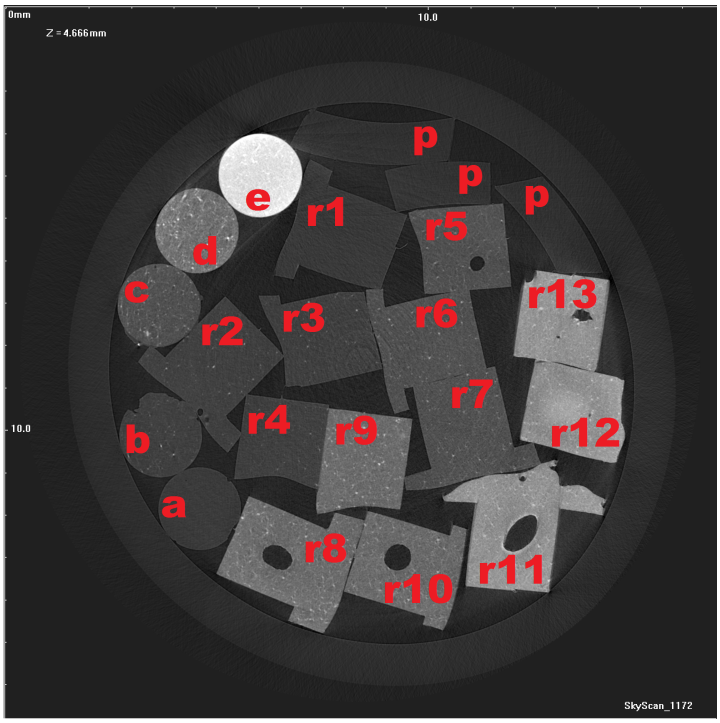

Figure 8.1: A slice from the image stack containing the samples r1–r13 used for testing the linear regression model. The commercial series of mineral calibration phantoms a–e are also imaged. The set is the same that has been imaged earlier. Plastic pieces placed purely for fixing purposes are marked as 'p'.

When the acquired data is fitted into the linear regression model, a representation of the correlation between the GV and BMD was determined as Y=0.037X – 576.920, as shown in Fig. 8.2. This representation can then be used for estimating BMD from a measured GV.

The mean grey scale levels determined for the prepared phantoms are now considered as parameters for the determined linear BMD estimation model. The RMS deviation of the data from the regression line is, as shown in the Fig. 8.2 above, given as in Equation 4.2

$$s_{y,x} = \sqrt{\frac{\sum (y_i - y_i')}{n-2}} = 9.900093 \approx 9.90.$$

The standard error s_{ye} of the estimated y_e is given by the Equation 4.3 and the standard error $s_{y'e}$ for a single predicted term y_e' by the equation 4.4. Implementing the values in these equations we get the estimated BMD

Table 8.1: Samples r1–r13 prepared for testing the linear regression model with the commercial set of mineral calibration phantoms. In this table the powder to liquid ratio is shown in terms of used dry powder mass per UV-glue resin. Three rods of each paste was produced to estimate the reproducibility. TV is for total volume and P/L stands for powder to liquid ratio.

Sample in scan	BMD (HAp/TV)	P/L (mg/1 ml)	Mean GV	SD	SE	CV (%)
r1	0	0.0	15 156	227	0.09	1.5
r2	24.8	25.0	16 154	315	0.13	2.0
r3	24.8	25.0	16 025	342	0.15	2.1
r4	24.8	25.0	16 112	304	0.14	1.9
r5	96.9	100.0	18 332	505	0.24	2.8
r6	96.9	100.0	18 278	466	0.21	2.6
r7	96.9	100.0	18 272	447	0.20	2.4
r8	231.7	250.0	22 027	794	0.36	3.6
r9	231.7	250.0	21 812	645	0.29	3.0
r10	231.7	250.0	21 683	642	0.30	3.0
r11	431.7	500.0	26 730	626	0.31	2.3
r12	431.7	500.0	26 654	875	0.51	3.3
r13	431.7	500.0	27 016	587	0.30	2.2
a	0		15 321	180	0.12	1.2
b	25		16 093	428	0.24	2.7
c	100		18 541	746	0.38	4.0
d	250		22 933	1 060	0.49	4.7
e	750		37 137	894	0.42	2.4

values with the error estimations as listed in Table 8.3. The σ_y is calculated as in Eq. 4.6.

Similarly we can now consider the measured grey scale levels for the commercial set of calibration phantoms as parameters of the determined BMD estimation model. The estimated BMD values can now be compared with the known reference BMD values given by the manufacturer. Results are listed in Table 8.4. Figure 8.3 shows the difference between the estimated BMD and the reference BMD given by the manufacturer.

Equation 4.5 gives us the precision error of an estimated Y' when the measurement X is subject to the precision error σ_{ex}. If we round up the

Table 8.2: The data used for the linear regression model.

BMD	Mean GV	GV	SE
0	15 172	479	0.07
24.8	16 102	684	0.09
96.9	18 277	938	0.14
231.7	21 851	1 335	0.18
431.7	26 807	1 472	0.21

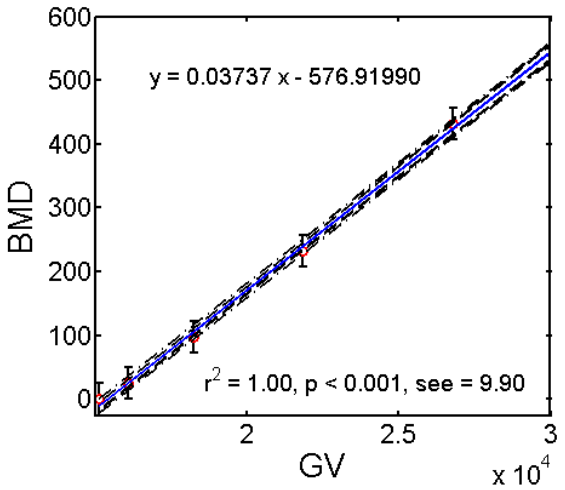

Figure 8.2: Data from Table 8.2 plotted with the determinded linear regression model. The correlation is significant. Error bars represent the reproducibility error as determined in Chapter 5.

highest standard error of Table 7.1 of the actual used sub volumes, we obtain $\sigma_{ex} = 5$. Now, if we overestimate the precision error over entire population to be 2 000, which is over double the measurement error of a single σ_x from Table 8.4, we get the term

$$\lambda/(1+\lambda) = 6 \cdot 10^{-6},$$

which differs from the λ itself only a little. If we now estimate the range of the measured BMD to be 1 000 mg/cc, which is a good estimate of BMD

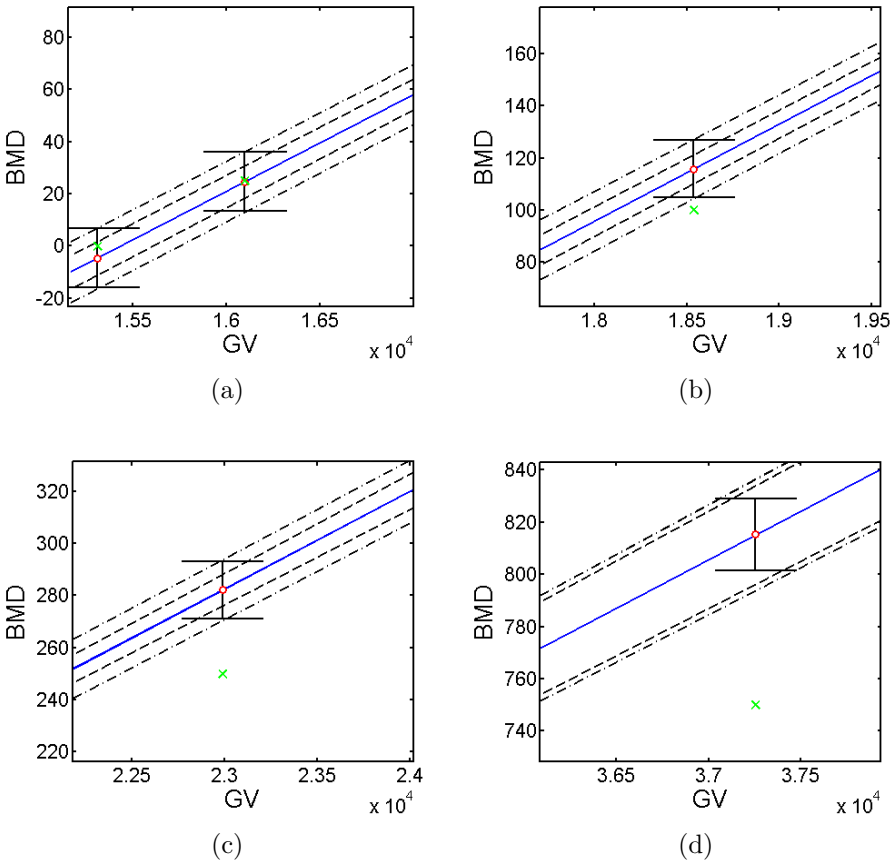

Figure 8.3: Linear regression model with the estimated (red dots) and actual data (green crosses) for the commercial mineral calibration phantom set (samples a–e). a) The difference between the estimated BMD and the manufacturer's value is insignificant for the small BMD (0 and 25 mg/cc). The model underestimates the 0 value by giving a negative value. The actual 0 value fits in the error limits. b) For actual BMD of 100 mg/cc and beyond the model overestimates the BMD. c) For actual BMD of 250 mg/cc the difference between actual value and the estimated value is roughly 13 %. d) Estimated value for 750 mg/cc is 9 % higher.

Table 8.3: The results for the estimated BMD values y' for produced phantom pastes. The s_{ye} and the $s_{y'e}$ represent the standard error of the prediction and standard error of a single estimation of the BMD value, respectively. These can be seen as inner and outer error limits in Fig. 8.2. σ_y is the standard deviation of the predicted term

GV	BMD	Estimated BMD y'	s_{ye}	$s_{y'e}$	σ_y
15 172	0	−9.9	6.4	11.8	$2.7 \cdot 10^{-3}$
16 102	24.8	24.8	5.8	11.5	$3.4 \cdot 10^{-3}$
18 277	96.9	106.1	4.7	10.9	$5.1 \cdot 10^{-3}$
21 851	231.7	239.7	5.0	11.1	$6.7 \cdot 10^{-3}$
26 807	431.7	424.8	8.7	13.2	$7.7 \cdot 10^{-3}$

Table 8.4: Results for implementing the acquired GV data for the commercial set of reference calibration phantoms.

GV	BMD = Y	Estimated BMD Y'	s_{ye}	$s_{y'e}$	σ_y
15 313	0	−4.7	6.4	11.8	$3.0 \cdot 10^{-3}$
16 098	25	24.6	5.8	11.5	$5.4 \cdot 10^{-3}$
18 539	100	115.9	4.7	10.9	$8.3 \cdot 10^{-3}$
22 986	250	282.1	5.0	11.1	$1.1 \cdot 10^{-2}$
37 254	750	815.3	8.7	13.2	$8.7 \cdot 10^{-3}$

of cortical bone, the term inside the square root becomes

$$\lambda/(1+\lambda) \cdot \sigma_y = 6 \cdot 10^{-6} \cdot 1\,000 = 6 \cdot 10^{-3}, \tag{8.1}$$

which is insignificant compared to the $s_{(y,x)}$ term. If we take the largest error for sub volume from the Table 7.1 to be $\sigma_{ex} = 130$, we would get inside the square root of Equation 4.5 the value

$$\lambda/(1+\lambda) = 4.2 \cdot 10^{-3}.$$

With this value the solution for equation 8.1 the precision error σ_{ex} is of the same order as $s_{(y,x)}$ and the estimate Y' is highly dependent on the precision

Table 8.5: The specifications of the developed bone mineral density calibration phantom pastes applied on the surface of a cortical bone sample.

Sample in scan	BMD	P/L (mg/1 ml)	Mean GV	SD	SE	CV (%)
b1	0.0	0.0	16 747	754.0	0.10	4.5
b2	100.0	103.3	18 928	1 980.5	0.15	10.5
b3	300.0	331.4	23 309	2 813.8	0.16	12.1

error. We must note that this happened only for the smallest of the virtual sub volumes that was tested for this method. The size of this particular sub volume is by no means relevant for the used method since it included only 74 pixels representing a cubic volume of $46.9 \cdot 10^{-9}$ cc representing width of a cube of 36 µm. Volume of this size is not practical for the final product of the evaluated method and thus can be disregarded.

As the error term can be simplified to only include the equation 4.4 for each grey value we measure, we can now determine the estimated BMD for any measured GV with a linear regression model.

8.2 Case example: BMD mapping in cortical bone

With the method presented above, BMD of a real cortical bone sample was studied by applying three different bone mineral density calibration phantoms on the surface of a bone sample. A linear BMD estimation model was then determined to correlate the measured GV and BMD.

The prepared phantom pastes were developed to contain 0, 100 and 300 mg/cc of HAp and the volume used would be small enough to contain the bone sample and the phantom pastes simultaneously on the field of view of 2.3 x 2.3 mm of the X-radia XCT-400 µCT device. The specifications of the prepared phantom pastes are listed in Table 8.5 along with the measured grey scale levels.

The bone sample used was extracted from cortical bone of a proximal anterior shaft of a cadaveric adult human femur. The age of a male donor was 82 years. The specimen was obtained by a medical and forensic autopsy, conducted at Department for Pathology, Kuopio University Hospital. The ethical permission was granted by the National Authority for Medicolegal

Figure 8.4: A sample of human cortical bone glued on a glass capillary ready for µCT imaging.

Affairs (TEO, 5783/04/044/07). A slice of cortical bone was cut below the minor trochanter. For µCT imaging the sample was extracted with a drill or a band saw, and was approximately 1–5 mm in diameter and less than 7 mm in length. The sample was stored individually in a phosphate buffered saline (PBS) solution (pH = 7.4) and kept frozen at a temperature of -80 °C during transportation and long storage. For my master thesis [8] a collection of these samples were prepared for µCT imaging by drying them separately in a freeze dryer Christ ALPHA 1-4 (Martin Christ, Osterode am Harz, Germany) in a 0.045 mbar vacuum (vacuum pump: Edwards RV3 H.P., Edwards High Vacuum International, Crawley, West Sussex, UK). The samples were cleaned of solid salts with compressed air and ground manually to fit the field of view of the µCT device.

The prepared pastes were applied separately on the surface of the bone sample and fixed with a handheld LED UV-light. Bone sample was glued to the tip of a glass capillary to help fixing the sample to the µCT device's sample stage (Fig. 8.4). Imaging parameters for the X-radia µCT were chosen by the manufacturer guidelines as: source/detector distance 25/5.5 mm, 10X magnification, 188° angle interval, 1 881 images, 60 s exposure time, source 35 kV and 4 W, reference every 10 images and filter LE1 used. For the 16-bit reconstruction parameters were: centershift -13.0, beam hardening 0.6, 3-section ring removal with bright and dark spot attenuation and applying Shepp-Logan function filter. A slice of the reconstructed CT data is shown in Fig. 8.5.

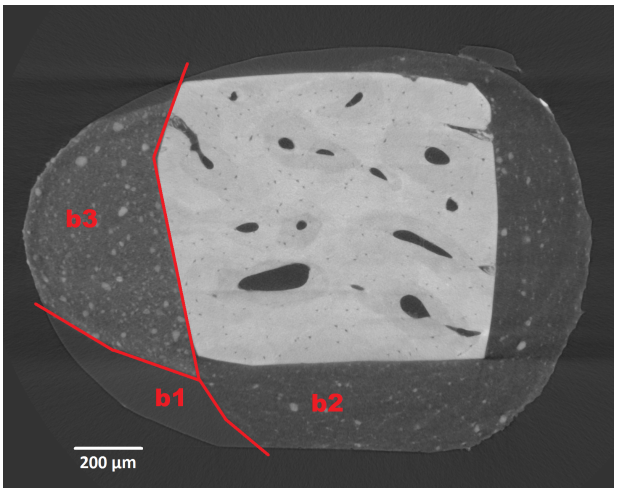

Figure 8.5: Reconstructed slice of cortical bone sample with the mineral calibration phantom pastes attached. Pastes are attached as follows: left side (light grey) b3 300 mg/cc, bottom and right side (darker grey) b2 100 mg/cc and bottom left corner (even composition) b1 0 mg/cc. The thickness of the b3 paste is about 440 µm.

Table 8.6: Results for the total bone volume mineral density estimation.

	Histogram GV	Linear regression model BMD
min	31 266	672.8
max	54 220	1 728.7
peak	49 984	1 382.0

Results

The GV data determined for the three phantom sub volumes were then used to fix the linear BMD estimation model, according to Section 8.1. Figure 8.6 shows the phantom GV-BMD data and the linear BMD estimation model determined.

For the bone volume imaged, the minimum, maximum and peak values of the GV level were determined (Fig. 8.7) and the values were then transformed by the linear BMD estimation model. Results are listed in Table 8.6.

Three sections of bone were cropped to evaluate BMD inside the bone

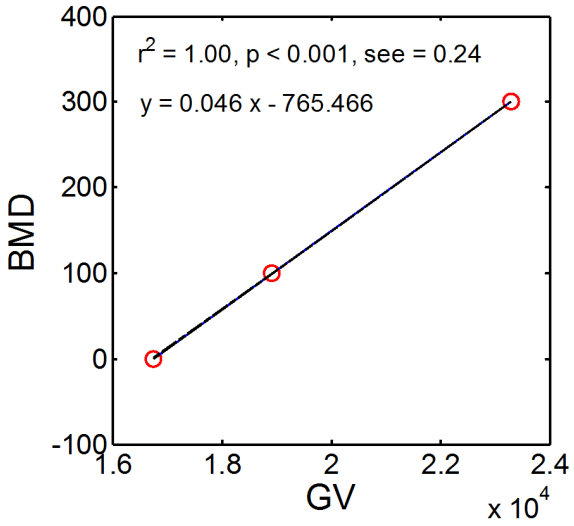

Figure 8.6: The linear regression model fitted with the phantom GV-BMD data. 'See' stands for standard error of estimation. Strong and significant linear correlation was observed for the phantom GV-BMD data.

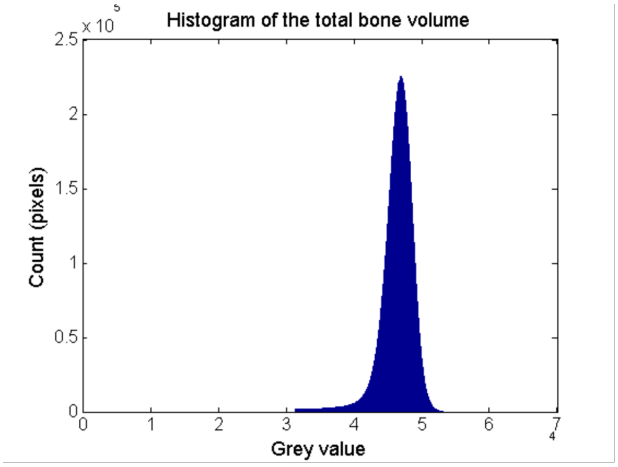

Figure 8.7: The histogram of the whole bone data imaged with the bone mineral density calibration pastes.

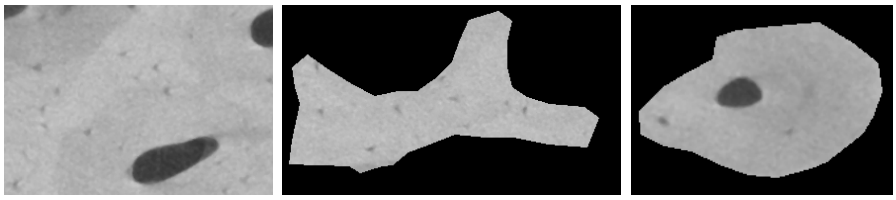

(a) (b) (c)

Figure 8.8: Slices showing the characteristics of the chosen subvolumes of cortical bone sample representing random average volume (a), intraosteonic volume (b) and osteonic volume (c). Total volumes for the chosen samples were $1.07 \cdot 10^{-4}$, $1.40 \cdot 10^{-5}$ and $2.51 \cdot 10^{-5}$ cc respectively.

Table 8.7: Acquired estimates for the chosen locations insinde the cortical bone sample.

Location	Mean GV	SD	SE	Estimated Y'	$s_{y'e}$
Site 1, average bone	45 617	7 604	0.90	1 319.7	0.48
Site 2, intraosteon	47 521	1 287	0.42	1 406.7	0.49
Site 3, osteon	43 570	1 786	0.46	1 226.1	0.49

matrix. Sections were chosen as follows: site number one represents common bone with varying bone density. No specific type was selected for this volume with a size of $74.5 \cdot 10^6$ pixels, or $1.07 \cdot 10^{-4}$ cc, including empty cavities such as Haversian canals. Site number two was selected to be of the intraosteon volume representing the higher end of the bone density range. Volume of the intraosteonic site was $9.7 \cdot 10^6$ pixels covering a volume of $1.40 \cdot 10^{-5}$ cc including lacunae. The third volume was selected to be osteonic volume as one randomly selected Haversian canal with its surroundings was chosen and cropped. The measured volume was $17.4 \cdot 10^6$ pixels, or $2.51 \cdot 10^{-5}$ cc including empty cavities. Selected slices representing the chosen volumes are illustrated in Fig. 8.8.

These volumes were thresholded and all empty cavities i.e. the Haversian and Volkmann canals and the lacunae, were extracted out of the investigated volume so they would not affect the BMD assessment. Inputting the measured bone GV data into the determined BMD estimation model provided BMD estimates as listed in Table 8.7 and shown in Figure 8.9.

The determined BMD estimation model was then used to map BMD of the imaged bone volume voxel by voxel. Fig. 8.10 shows a slice of the

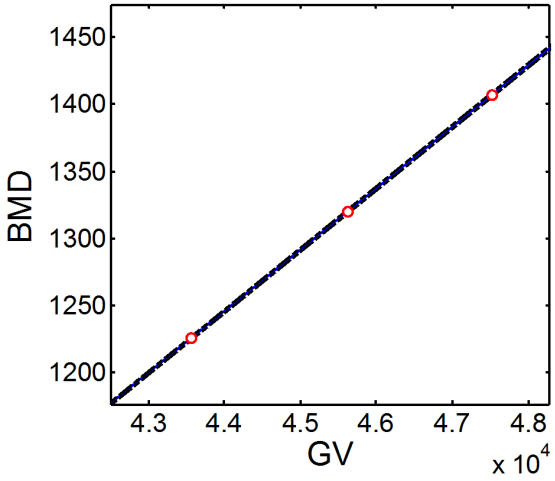

Figure 8.9: Acquired grey scale levels in three phantom subvolumes gives the estimation of BMD in a cortical bone sample.

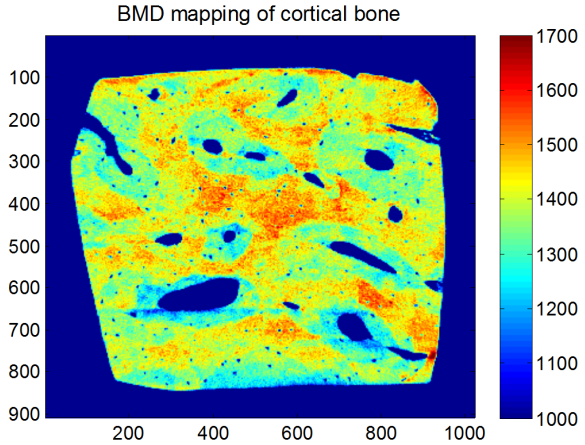

Figure 8.10: A slice of the reconstructed cortical bone sample with BMD mapping (scale in mg/cc). Note that the slice is exactly the same as in Fig. 8.5.

cortical bone mapped for the BMD scale, represented as milligrams per cubic centimeter of bone mineral. Fig. 8.11 shows BMD mapping of the slices shown in Fig. 8.8.

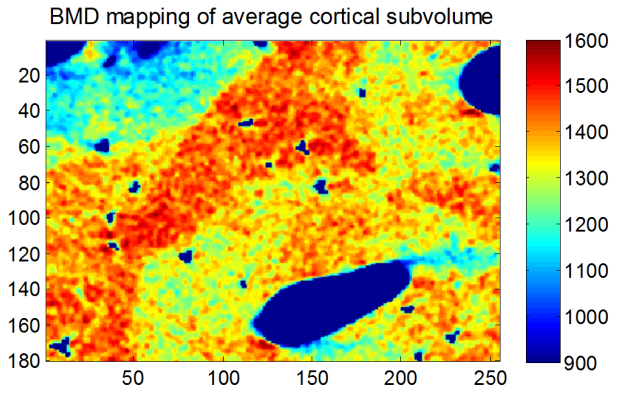

(a)

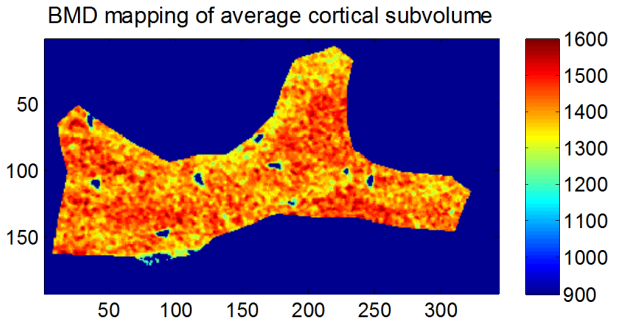

(b)

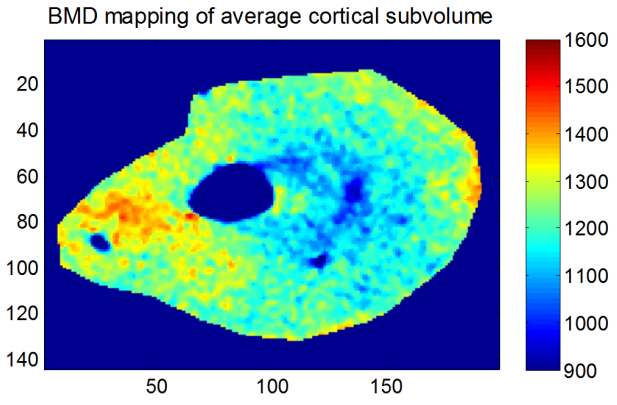

(c)

Figure 8.11: BMD mapping of the chosen sub volumes shown in Fig. 8.8 representing random average volume (a), intraosteonic volume (b) and osteonic volume (c). Identical color scale (mg/cc) was used.

Chapter 9

Discussion

This thesis introduced a novel method to solve the volume limitation of phantom-based calibration of bone mineral density in high-resolution microtomography. While commercially available phantoms are, in general, too large to fit the field of view at the millimeter scale, development of customized phantoms was needed. To this end, we developed a paste-like bone mineral density phantom which permits thin coating of the bone sample. A mixture of hydroxyapatite powder and UV curing adhesive was shown to be an adequate composition for such a phantom. The recipe of phantom preparation was shown to be reproducible and the paste material was shown temporally stable within at least the two week time frame analyzed. The quality of the phantoms was shown similar or better than that of the commercially available phantoms tested. Despite apparent inhomogeneity within the phantom medium, the reference grey scale level was represented with sufficient accuracy down to at least a 0.05 mm^3 limit of the phantom volume. In particular, preliminary tests by three distinct phantom grey scale levels suggest excellent feasibility of mapping the bone mineral density scale of real human cortical bone.

Volumetric bone mineral density in small scale has not been extensively studied due to practical difficulties. It has been shown that the mineral density varies greatly inside the bone matrix. In addition, there are major fluctuations even between osteons lying next to each other, not to mention the intraosteon volumes in between. Haversian system and the bone medullary canal is where most of the metabolic activity lies, and these are also sites for the mineral reserve to be first disassembled. Understanding the distribution of the mineral content in micrometer scale might give us a hint of how bone strength is constructed, not only by geometrical features but also by the apparent features of varying density. In addition to the mechanical properties of bone this could explain the propagation of ultrasonic

waves [80] in more detail.

Different mineral pastes have been made [71, 81] in previous studies. These pastes have mainly been designed to be applied on the fracture sites of bones to study the resorption of calcium from the applied mass to the formation of bone matrix or to mimic bone material in tensile strength studies. However, these pastes did not meet the requirements set in the present work. A new formula was thereby developed with special attention paid in simplicity and the granular composition of the paste.

The original idea was to produce a phantom made of the same components than cortical bone. It became evident, however, that mixing hydroxyapatite with organic bonding agents and conserving the paste were difficult. The paste recipe with no organic components and with UV resin was a major achievement of this work. An ultrasonic processor was also found very useful in producing the paste.

During the work, it became evident that the two requirements for calibration standard mentioned in Section 4.1 could not be fully satisfied. The first requirement, concerning similar X-ray attenuation, was covered by using hydroxyapatite as the mineral substitute. This was proven by spectrometric experiments where very similar absorption spectra was found (see Section 4.2). The density and thus the total absorption level typical to cortical bone was not reached, however. Estimating the density of bone tissue using the present phantom material thus requires linear extrapolation of the calibration results. Naturally this may lower the reliability of the estimated condition of bone. The second requirement about homogeneity of the sample was partially met.

The actual linear regression model that was tested for fixed phantom rods produced a decent estimation of the mineral density values present inside the commercial phantom set that was used as a test material. The model was fitted against 5 data points and gave good accuracy for the lower bone mineral density values. The higher the calibration phantom mineral density levels rose, the more the regression model gave over estimated results. At the top end for the 750 mg/cc phantom the difference was 9 % and the error estimation did not include the actual result measured directly from the grey value.

The choice of using UV curing adhesive was backed by the ease of operation comparing to other possible solutions. Epoxy resin for instance is a common binding material used in the making of mineral calibration phantoms. As a two component adhesive the mixing of paste beforehand is pointless as the epoxy needs the hardener part to solidify. This leads to quick mixing of the paste materials before fixing on the surface of the studied sample, which then compromises the homogeneity of the paste material.

Thus choosing UV curable resin was a good way of having the mineral calibration phantom as wet paste form until fixing. The paste was easy to apply and the amount and shape of the paste could be adjusted manually before fixing with aid of an optical microscope. Plain UV resin was noted as water equivalent which could be used as a zero point for the mineral regression line.

The quality of the produced phantom paste was tested in various ways. Different methods to demonstrate the stability of both the production routine and the qualitative features of the used paste and fixed phantom rods were performed including repetitive testing and analysis. At first the phantoms were prepared in larger scale with dimensions of 2 x 2 x 10 mm due to easier handling and similar dimensions with commercially available phantoms to allow comparison. Imaging with lower resolution by using the Skyscan µCT allowed faster operation times and better response for development of the phantom material. Imaging made throughout Chapters 5 – 7 resulted in identical GV values with similar SD and CV values (around 1000 units and approximately 5 %, respectively). Largest aggregates of hydroxyapatite were measured to be about 70 µm in diameter which was similar with previous observations.

During the mineral density calibration of a cortical bone sample in Chapter 8.2 the size of the used phantoms was reduced to suit the FOV of the X-radia µCT device. While the quality of the phantom paste remained identical to previous tests, as mineral aggregates were measured to be of same size as in the previous chapters, results in the range of GV values changed due to different µCT. This can be detected from the values of SD and CV which where doubled. The reason for this increase is due to better resolution and smaller pixel size that enhance the undesirable effects of the inhomogeneity thus increasing the measurement error and decreasing the reliability of the used method. Imaging with lower resolution suppresses the unmixed aggregates that are smaller than the spatial resolution of the µCT but also conceals the microscopic structure and fine density alterations in the target sample e.g. cortical bone.

Three bone volumes representing different tissue types were then selected to be fitted in the linear regression model. Volumes were an average small bone volume and corresponding volumes of osteonal and intraosteonal volumes. As seen in Fig. 8.9 different mineral densities were acquired for these volumes. The osteonal and intraosteonal values differed nearly 15 % of each other. The average bone volume is located conveniently in between the two extreme values. Taken into account all recognized sources of error, the estimated bone mineral value can be up to 20 % higher than the actual value. A mean result of 1 382 mg/cc was acquired for the total volume of the

studied cortical bone sample. Although a little high, this value fits on the range of average cortical density [25, 26, 27]. For the chosen volumes (sub volumes 1–3) actual mineral density was never measured with any reference method.

The cortical bone sample studied in this work shows the effectiveness of the mineral pastes (Fig. 8.5, 8.10). The sample was obtained from an 82 year old male and showed lower than average values of structure model index, trabecular thickness and degree of anisotropy [5]. The cadaver was not diagnosed with osteoporosis. Based on this study alone one cannot say if the bone properties of this exact specimen are outside the normal spread in age related bone loss. Evidently, as seen from the images mentioned earlier, the bone matrix in intraosteon volume is denser than inside an osteon. Osteonic bone tissue is younger and thus less dense and it is known that the metabolism is more active in the bone marrow cavity and inside Haversian canals of which the osteons are concentrically aligned. Thus lower density could also be due to the increased resorption of bone mineral matrix. This question, however, remains unanswered.

In the future the method presented in this work should be applied to a larger group of samples in order to know if this kind of behaviour in the density of the cortical bone has any statistical reference. Samples would be needed both from a group with diagnosed osteoporosis and from a control group to possibly identify clear differences in bone properties, especially the mineral density inside osteonal and intraosteonal volumes.

Final words

The characteristic nature of experimental physics can sometimes be cruel to its maker. It is not uncommon that a great deal of work is left unwritten, unpublished and so unnoticed. Starting something from scratch usually means lots of learning by trial and error. So it was with this study.

The idea of creating yet another type of phantom to be used in the evaluation of mineral density in bone started from a common idea and was supposed to be a quick job and a small part of something bigger. Soon it became clear that this was not an easy task nevertheless. Hundreds of samples was created, ruined, tossed into the garbage and started all over again. The final objective in mind new ways to approach the problem was tried as they were innovated. Usually this was done by confronting yet another problem of sample instability in some manner. It is strange how often the simple tasks require profound examination to be solved correctly and how the complex measurements can be the most straightforward to accomplish.

Still this study has achieved better understanding of bones histomorphology properties. In my master thesis ([8]) the difference between the osteonal and intraosteon volume was detected but could not be evaluated at given time. At this resolution the measured difference of 15 % is significant especially if we have an estimate of a real anatomical value, the volumetric bone mineral density which is often used to measure body's composition and condition. With the given method it is possible to assess both the morphometric and density analysis in high resolution at the same time without the need for separate imaging techniques or other measurements. By this method we can especially avoid the total destruction of the bone sample since there is no need for ashing. The final question that this study leaves for later surveys is, how the mineral content dissolves from the bone matrix and what is the bone mineral density ratio between osteon and intraosteon volume in bone.

References

[1] E. Curtis, A. Litwic, C. Cooper, and E. Dennison. Determinants of muscle and bone aging. *J. Cell. Physiol.*, 230:2618–2625, 2015.

[2] E. Hernlund, A. Svedbom, M. Ivergard, and *et al.* Osteoporosis in the european union: Medical management, epidemiology and economic burden. a report prepared in collaboration with the international osteoporosis foundation (iof) and the european federation of pharmaceutical industry associations (efpia). *Arch Osteoporos*, 8(136), 2013.

[3] R. D. Wasnich. Epidemiology of osteoporosis. In M. J. Favus, editor, *Primer on the Metabolic Bone Diseases and Disorders of Mineral Metabolism*. Lippincott, Williams and Wilkins, Philadelphia, fourth edition, 1999.

[4] J. Karjalainen. *Novel Pulse-Echo Ultrasound Methods for Diagnostics of Osteoporosis*. PhD thesis, University of Eastern Finland, 2011.

[5] M.K.H. Malo, D. Rohrbach, H. Isaksson, and *et al.* Longitudinal elastic properties and porosity of cortical bone tissue vary with age in human proximal femur. *Bone*, 53:451–458, 2013.

[6] B. Hesse, N. Männicke, A Pacureanu, and *et al.* Accessing osteocyte lacunar geometrical properties in human jaw bone on the submicron length scale using synchrotron radiation μct. *Journal of Microscopy*, 255(3), 2014.

[7] J. M. Deuerling, D. J. Rudy, and R. K. Niebur, G. L. abd Roeder. Improved accuracy of cortical bone mineralization measured by polychromatic microcomputed tomography using a novel high mineral density composite calibration phantom. *Med. Phys.*, 37(9):5138–45, 2010.

[8] J. Pirhonen. Morphological analysis of human cortical bone using high-resolution x-ray microtomography. Master's thesis, University of Jyväskylä, 2012.

[9] S. Schweizer, B. Hattendorf, and *et al.* Preparation and characterization of calibration standards for bone density determination by micro-computed tomography. *Analyst*, 132:1040–1045, 2007.

[10] B. Clarke. Normal bone anatomy and physiology. *Clin J Am Soc Nephrol*, 3:S131–S139, 2008.

[11] R. Baron. Anatomy and ultrastructure of bone. In M. J. Favus, editor, *Primer on the Metabolic Bone Diseases and Disorders of Mineral Metabolism*. Lippincott, Williams and Wilkins, Philadelphia, fourth edition, 1999.

[12] K. L. Moore and A. F. Dalley. *Clinically oriented anatomy*. Lippincott, Williams and Wilkins, Baltimore, fifth edition, 2006.

[13] H. Gray and W. H. Lewis. *Anatomy of the Human Body*. Bartleby, New York, NY, USA, 20 edition, 1918 / 2000.

[14] V. K. Sarin, G. M. Erickson, N. J. Giori, A. G. Bergman, and D. R. Carter. Coincident development of sesamoid bonesand clues to their evolution. *Anat Rec (New Anat)*, 257:174–180, 1999.

[15] G. R. Mundy. Bone remodelling. In M. J. Favus, editor, *Primer on the Metabolic Bone Diseases and Disorders of Mineral Metabolism*. Lippincott, Williams and Wilkins, Philadelphia, fourth edition, 1999.

[16] C. T. Rubin and J. Rubin. Biomechanics of bone. In M. J. Favus, editor, *Primer on the Metabolic Bone Diseases and Disorders of Mineral Metabolism*. Lippincott, Williams and Wilkins, Philadelphia, fourth edition, 1999.

[17] R. B. Martin, D. B. Burr, and N. A. Sharkey. *Skeletal Tissue Mechanics*. Springer-Verlag New York Inc., New York, 1998.

[18] J. D. Currey. *Bones: structure and mechanics*. Princeton University Press, USA, 2002.

[19] J-Y. Rho, L. Kuhn-Spearing, and P. Zioupos. Mechanical properties and the hierarchial structure of bone. *Medical Engineering & Physics*, 20:92–102, 1998.

[20] J. A. Buckwalter, M. J. Glimcher, R. R. Cooper, and R. Recker. Bone biology. part I: structure, blood supply, cells, matrix, and mineralization. *J Bone and Joint Surg*, 77-A:1256–1275, 1995.

[21] F. Kaplan, W. Hayes, T. Keaveny, and *et al.* Form and function of bone. In S. Simon, editor, *Orthopaedic basic science*. American academy of orthopaedic surgeons, Columbus, 1994.

[22] J. B. Lian, G. S. Stein, and *et al.* Bone formation: Osteoblast lineage cells, growth factors, matrix proteins, and the mineralization process. In M. J. Favus, editor, *Primer on the Metabolic Bone Diseases and Disorders of Mineral Metabolism*. Lippincott, Williams and Wilkins, Philadelphia, fourth edition, 1999.

[23] J. Ren, I. Dimitrov, A. D. Sherry, and C. R. Malloy. Composition of adipose tissue and marrow fat in humans by ^{1}H NMR at 7 Tesla. *J Lipid Res.*, 49(9):2055–2062, 2008.

[24] C. A. Beevers and D. B. McIntyre. The atomix structure of fluorapatite and its relation to that of tooth and bone mineral. *Miner. Mag.*, 27:254–9, 1956.

[25] C. B. Smith and D. A. Smith. Relations between age, mineral density and mechanical properties of human femoral compacta. *Acta Orthopaedica Scandinavica*, 47(5):496–502, 1976.

[26] C. H. Turner, M. Sato, and H. U. Bryant. Raloxifene preserves bone strength and bone mass in ovariectomized rats. *Endocrinology*, 135(5), 1994.

[27] E. M. S. Tam, F. W. P. Yu, V. W. Y. Hung, and *et al.* Are volumetric bone mineral density and bone microarchitecture associated with leptin and soluble leptin receptor levels in adolescent idiopathic scoliosis? – a case-control study. *PLoS ONE*, 9(2: e87939), 2014.

[28] J. D. Currey. The structure and mechanics of bone. *J Mater Sci*, 47:41–54, 2011.

[29] H.D. Young and R.A. Freedman. *Sears and Zemansky's University Physics*. Pearson education Inc., Addison Wesley, San Francisco, USA, 11 edition, 2004.

[30] D. J. Hadjidakis and I. I. Androulakis. Bone remodeling. *Ann. N.Y. Acad. Sci.*, 1092:385–396, 2006.

[31] J. Clifford, M. D. Rosen, and P. Douglas. The aging skeleton. In M. J. Favus, editor, *Primer on the Metabolic Bone Diseases and Disorders of Mineral Metabolism*. Lippincott, Williams and Wilkins, Philadelphia, fourth edition, 1999.

[32] B. R. Olsen. Bone morphogenesis and embryologic development. In M. J. Favus, editor, *Primer on the Metabolic Bone Diseases and Disorders of Mineral Metabolism*. Lippincott, Williams and Wilkins, Philadelphia, fourth edition, 1999.

[33] R. A. Chen and W. G. Goodman. Role of the calcium-sensing receptor in parathyroid gland physiology. *American Journal of Physiology - Renal Physiology*, 286(6):F1005–F1011, 2004.

[34] Anonymous. Consensus developmentconference: diagnosis, prophylaxis and treatment of osteoporosis, 1993.

[35] R. Lindsay and F. Cosman. Prevention of osteoporosis. In M. J. Favus, editor, *Primer on the Metabolic Bone Diseases and Disorders of Mineral Metabolism*. Lippincott, Williams and Wilkins, Philadelphia, fourth edition, 1999.

[36] A. M. Parfitt. Age-related structural changes in trabecular and cortical bone: cellular mechanisms and biochemical consequences. *Calcif Tissue Int*, 36(1):S123–S128, 1984.

[37] R. M. D. Zebaze, A. Ghasem-Zadeh, A. Bohte, and *et al.* Intracortical remodelling and porosity in the distal radius and post-mortem femurs of women: a cross-sectional study. *Lancet*, 375:1729–36, 2010.

[38] R. Eastell. Pathogenesis of postmenopausal osteoporosis. In M. J. Favus, editor, *Primer on the Metabolic Bone Diseases and Disorders of Mineral Metabolism*. Lippincott, Williams and Wilkins, Philadelphia, fourth edition, 1999.

[39] C. R. Rosen. Anatomy, physiology and disease. In C. M. Langton and C. F. Njeh, editors, *The Physical Measurement of bone*. Institute of Physics Publishing, Bristol, UK, 2004.

[40] P. Moilanen. *Ultrasonic guided wave measurements in bone*. Department of Physics, University of Jyväskylä, 2004. Research Report No. 8/2004.

[41] M. A. Moyad. Osteoporosis: a rapid review of risk factors and screening methods. *Urologic Oncology: Seminars and Original Investigations*, 21:375–379, 2003.

[42] WHO Scientific Group. Prevention and management of osteoporosis. WHO Technical Report Series 921, World Health Organization, Geneva, 2003.

[43] R. Brunader and D. K. Shelton. Radiologic bone assessment in the evaluation of osteoporosis. *Am Fam Physician*, 1;65(7):1357–1365, 2002.

[44] K. Raum, Q. Grimal, P. Varga, R. Barkmann, C. C. Glüer, and P. Laugier. Ultrasound to assess bone quality. *Curr Osteoporos Rep*, 12:154–162, 2014.

[45] O. Pukkila. *Säteily ja ydinturvallisuus, osa 3: Säteilyn käyttö*. Säteilyturvakeskus, Hämeenlinna, 2004.

[46] G. Landwehr. In A. Hasse, editor, *Röntgen centennial: X-rays in Natural and Life Sciences*. World Scientific, Singapore, 1997.

[47] A. Haavisto, L. Karkela, M. Kervinen, and *et al. maol-taulukot*. Otava, Keuruu, 2001. 1-3. uudistettu painos.

[48] A. G. Webb. *Introduction to Biomedical Imaging*. Number 1. Wiley-iEEE Press, 2003.

[49] A Thompson and *et al. X-Ray Data Booklet*. Lawrence Berkeley National Laboratory, University of California, Berkeley, CA 94720, USA, 2009.

[50] R.P.C. Schram. X-ray attenuation, 2011. 20002/01.44395/I.

[51] M. Cooper. X-ray compton scattering. *Phys. Educ.*, 7, 1972.

[52] W. Zou, N. Hunter, and M. V. Swain. Application of polychromatic μCT for mineral density determination. *J Dent Res*, 90(1):18–30, 2011.

[53] F. Natterer. *The Mathematics of Computerized Tomography*. SIAM, Philadelphia, 2001.

[54] F. Natterer and F. Wübbeling. *Mathematical Methods in Image Reconstruction*. SIAM, Philadelphia, 2001.

[55] T. Hildebrand and P. Rüegsegger. Quantification of bone microarchitecture with the structure model index. *CMBBE*, 1:15–23, 1997.

[56] E. Martín-Badosa, A. Elmoutaouakkil, S. Nuzzo, and *et al.* A method for the automatic characterization of bone architecture in 3d mice microtomographic images. *Computerized Medical Imaging and Graphics*, 27:447–458, 2003.

[57] *High-resolution in-vivo micro-CT scanner for small animals*, volume 4503, 2002.

[58] H. van Lenthe, T. L. Mueller, A. J. Wirth, and R. Müller. Quantification of bone structural parameters and mechanical competence at the distal radius. *J Orthop Trauma*, 22(8), 2008.

[59] B. Hesse, P. Varga, M. Langer, and *et al.* Canalicular network morphology is the majordeterminant of the spatial distribution of mass densityin human bone tissue: Evidence by means ofsynchrotron radiation phase-contrast nano-ct. *Journal of Bone and Mineral Research*, 30(2), 2015.

[60] R. Gonzáles-García and F. Monje. The reliability of cone-beam computed tomography to assess bone density at dental implant recipient sites: a histomorphometric analysis by micro-ct. *Clin. Oral Impl. Res.*, 24:871–879, 2012.

[61] MA USA Bruker Corporation, Billerica. Analysis of bone by micro-ct general information. Method Note.

[62] C. Cui, S. M. Jorgensen, D. R Eaker, and E. L. Ritman. Direct three-dimensional coherently scattered x-ray microtomography. *Med. Phys.*, 37(12):211–219, 2010.

[63] K. Raum, I. Leguerney, F. Chandelier, and *et al.* Site-matched assessment of structural and tissue properties of cortical bone using scanning acoustic microscopy and synchrotron radiation μCT. *Phys. Med. Biol.*, 51:733–746, 2006.

[64] Computerized Imaging Reference Systems Inc. `http://www.cirsinc.com/products/modality/27/micromouse-and-water-filled-mouse-phantoms/`. Date of reference: 10.12.2015.

[65] QRM Quality Assurance in Radiology and Medicine GmbH. `http://www.qrm.de/content/products/microct/microct_ha.htm`. Date of reference: 10.12.2015.

[66] A. Nazarian, B. D. Snyder, D. Zurakowski, and R. Müller. Quantitative micro-computed tomography: A non-invasive method to assess equivalent bone mineral density. *Bone*, 43:302–311, 2008.

[67] P. Szpak. Fish bone chemistry and ultrasturcture: Implications for taphonomy and stable isotope analysis. *Journal of Archaeological Science*, 2011.

[68] W.M. Haynes, editor. *CRC Handbook of Chemistry and Physics*. CRC Press LLC, Boca Raton: FL, USA, 94 edition, 2013-2014.

[69] Permabond® Engineering Adhesives. Permabond® uv630 uv-curable adhesive.

[70] J. W. Anthony, R. A. Bideaux, K. W. Bladh, and M. C. Nichols. *Hydroxylapatite. Handbook of Mineralogy (PDF). IV (Arsenates, Phosphates, Vanadates)*. Mineralogical Society of America, Chantilly, VA, US, 2000 edition, 2000.

[71] T. Chae. Processing and characterization of hydroxyapatite-based bioceramic pastes. Master's thesis, The University of British Columbia, 2007.

[72] Sonics & Materials, Inc., Newton, CT, USA. *Sonics vibra-cell™ High Intensity Liquid Processors*, 2015.

[73] Xradia, Inc., Concord, CA. *Xradia MicroXCT-200 and MicroXCT-400 User's Guide*, version 7.0, revision 1.5 edition, 2010.

[74] Skyscan N.V., Aartselaar, Belgium. *Desktop X-ray microtomograph - Instruction Manual*, 2005.

[75] Bruker microCT. `http://bruker-microct.com/products/1172.htm`. Date of reference: 14.12.2015.

[76] Xcom database. `http://physics.nist.gov/PhysRefData/Xcom/html/xcom1.html`. National Institute of Standards and Technology (NIST), 100 Bureau Drive, Stop 1070, Gaithersburg, MD, USA, Date of reference: 7.10.2015.

[77] J. H. Hubbell and S. M. Seltzer. Tables of x-ray mass attenuation coefficients and mass energy-absorption coefficients from 1 kev to 20 mev for elements z = 1 to 92 and 48 additional substances of dosimetric interest*, 1993.

[78] W. Zou, J. Gao, A. S. Jones, N. Hunter, and M. V. Swain. Characterization of a novel calibration method for mineral density determination of dentine by x-ray micro-tomography. *Analyst*, 134:72–79, 2009.

[79] G. W. Snedecor. *Statistical methods*. The Iowa State University Press, Ames, Iowa, USA, 6 edition, 1976.

[80] P. Moilanen. Ultrasonic guided waves in bone. *IEEE Transactions on Ultrasonics, Ferroelectrics, and Frequency Control*, 55(6):1277–1286, 2008.

[81] S. Aghyarian, L. C. Rodriguez, J Chari, and *et al.* Characterization of a new composite pmma-ha/brushite bone cement for spinal augmentation. *Journal of Biomaterials Applications*, 29(5):688–698, 2014.

And if I recover
Will you be my comfort
Or it can be over
Or we can just leave it here
So pick any number
Choose any color
I've got the answer
Open the envelope

— CHVRCHES